



**HAL**  
open science

# Nonlinear broadband time-domain admittance boundary condition for duct acoustics. Application to perforated plate liners

Daher Diab, Didier Dragna, Edouard Salze, Marie-Annick Galland

► **To cite this version:**

Daher Diab, Didier Dragna, Edouard Salze, Marie-Annick Galland. Nonlinear broadband time-domain admittance boundary condition for duct acoustics. Application to perforated plate liners. *Journal of Sound and Vibration*, 2022, 528, pp.116892. 10.1016/j.jsv.2022.116892 . hal-04736437

**HAL Id: hal-04736437**

**<https://hal.science/hal-04736437v1>**

Submitted on 13 Nov 2024

**HAL** is a multi-disciplinary open access archive for the deposit and dissemination of scientific research documents, whether they are published or not. The documents may come from teaching and research institutions in France or abroad, or from public or private research centers.

L'archive ouverte pluridisciplinaire **HAL**, est destinée au dépôt et à la diffusion de documents scientifiques de niveau recherche, publiés ou non, émanant des établissements d'enseignement et de recherche français ou étrangers, des laboratoires publics ou privés.



Distributed under a Creative Commons Attribution - NonCommercial 4.0 International License

# Nonlinear broadband time-domain admittance boundary condition for duct acoustics. Application to perforated plate liners.

Daher Diab, Didier Dragna, Edouard Salze, Marie-Annick Galland

*Univ Lyon, Ecole Centrale de Lyon, CNRS, Univ Claude Bernard Lyon 1, INSA Lyon, LMFA, UMR5509, 69130, Ecully, France*

---

## Abstract

The behavior of perforated plates at high excitation level is generally modelled by a surface impedance that depends on the rms velocity in the perforations. A time-domain admittance boundary condition (TDABC) is developed to account for this variation using a multipole model. Two formulations are considered, based on the interpolation either of the admittance or of the multipole coefficients from a data set of reference values. These TDABC are implemented in a finite-difference time-domain solver of the linearized Euler equations and are validated by comparison with experimental results on an impedance tube. Application to a two-dimensional lined duct corresponding to the reference geometry of the NASA Grazing Incidence Tube is then performed. The spatial variation of the perforated plate liner impedance is highlighted and it is shown that assuming a uniform impedance can lead to an unacceptable prediction of the liner attenuation. These results are confirmed both for a harmonic or broadband excitation.

*Key words:* Nonlinear admittance, perforated panel, time-domain simulation, time-domain admittance boundary condition, spatially-varying admittance

---

## 1. Introduction

Acoustic liners are widely used for noise reduction in several industrial applications such as nacelles of aircraft engines, exhaust ducts or air ventilation systems. Among them, the perforated plate (PP) liner is probably the most employed, because of its simplicity, its efficiency and its applicability to extreme environmental conditions (temperature and pressure) where porous materials cannot be used. It is made of a perforated plate, mounted on a honeycomb cavity attached to the system frame. This liner behaves as a resonator. As such, PP liners provide a significant acoustic

---

*Email addresses:* [daher.diab@ec-lyon.fr](mailto:daher.diab@ec-lyon.fr) (Daher Diab), [didier.dragna@ec-lyon.fr](mailto:didier.dragna@ec-lyon.fr) (Didier Dragna), [edouard.salze@ec-lyon.fr](mailto:edouard.salze@ec-lyon.fr) (Edouard Salze), [marie-annick.galland@ec-lyon.fr](mailto:marie-annick.galland@ec-lyon.fr) (Marie-Annick Galland)

*Preprint submitted to Elsevier*

*February 16, 2022*

1  
2  
3  
4  
5  
6  
7  
8  
9  
10  
11  
12  
13  
14  
15  
16  
17  
18  
19  
20  
21  
22  
23  
24  
25  
26  
27  
28  
29  
30  
31  
32  
33  
34  
35  
36  
37  
38  
39  
40  
41  
42  
43  
44  
45  
46  
47  
48  
49  
50  
51  
52  
53  
54  
55  
56  
57  
58  
59  
60  
61  
62  
63  
64  
65

8 attenuation, but only near the resonant frequencies that depend mainly on the cavity depth.

9 Starting from Sivian [1], it has been noted that the perforated plate excited by an acoustic  
10 wave with a large amplitude exhibits a nonlinear behavior. More precisely, the measured acoustic  
11 impedance was shown to depend on the rms velocity in the perforation. This behavior is associated  
12 to the flow separation that occurs at the perforation edges for a sufficiently large amplitude of  
13 the velocity in the perforation. This induces generation of vortices and conversion of acoustic  
14 energy into vortical energy, which results in an increase of the plate resistance. Even for moderate  
15 SPL (around 110-120 dB), at which sound propagation remains a linear process, perforated plates  
16 can exhibit a nonlinear behavior. In ducted systems, such as engine nacelles, the sound pressure  
17 level (SPL) can be much higher. In such conditions, the nonlinear response of PP liners must be  
18 accounted for.

19 Detailed direct numerical simulations of the flow in a perforated liner excited by an acoustic  
20 wave with a large amplitude have been already performed [2, 3]. Due to their high computational  
21 cost, they are however limited to simple configurations. For predicting the sound attenuation  
22 brought by a whole panel, it is more suitable to rely on numerical simulations in which the acoustic  
23 behavior of the perforated liner is modeled.

24 To do so, the most common approach is to employ a surface impedance model of the perforated  
25 plate liner, that includes nonlinear effects. It should be noted that the concept of surface impedance  
26 is strictly valid in the linear regime. It can be extended for a sinusoidal excitation in the nonlinear  
27 regime without difficulty, as long as the harmonic distortion remains limited. In the other cases,  
28 especially for a broadband excitation, the surface impedance in the nonlinear regime has to be used  
29 carefully. Several semi-empirical models for surface impedance of perforated plate liners [4–9] have  
30 been proposed. In most of them, based on measurements reported in the literature (among others  
31 Refs. [10, 11]), the nonlinear correction consists in an increase of the resistance and a decrease  
32 of the orifice end correction, with the amplitude of the acoustic velocity in the orifice. Recently,  
33 Laly et al. [12] have extended in the nonlinear regime the model developed by Atalla and Sgard  
34 [13] based on an equivalent fluid approach to represent perforated panels: the resistivity and the  
35 tortuosity of the equivalent fluid depends on the geometrical properties of the perforated plate as  
36 well as the amplitude of the acoustic velocity in the perforation. An other approach proposed by  
37 Cummings [14] is to directly relate the pressure jump at the perforated plate and the velocity in  
38 the perforation through a nonlinear differential equation in the time-domain.

39 Nevertheless, there are few attempts to account for nonlinear models of PP liners in numerical

1  
2  
3  
4  
5  
6  
7  
8  
9  
10  
11  
12  
13  
14  
15  
16  
17  
18  
19  
20  
21  
22  
23  
24  
25  
26  
27  
28  
29  
30  
31  
32  
33  
34  
35  
36  
37  
38  
39  
40  
41  
42  
43  
44  
45  
46  
47  
48  
49  
50  
51  
52  
53  
54  
55  
56  
57  
58  
59  
60  
61  
62  
63  
64  
65

simulations of sound propagation in lined ducts. One can refer to Eversman [15] or, more recently, to Roncen *et al.* [16], that use frequency-domain approaches to investigate the effect of nonlinearity on liner performance in a flow duct. While frequency-domain methods can still be used for a high-level harmonic excitation, time-domain methods are the natural approach to account for nonlinear effects. In the time-domain, the impedance boundary condition translates into a convolution, whose direct numerical evaluation is time-consuming [17]. A vast literature thus aimed at proposing time-domain impedance or admittance boundary conditions (TDIBC or TDABC) in the linear regime (e.g. [17–21]). Among the proposed approaches, TDIBC based on the multipole model has attracted lot of attention [19, 22–24], as it can be used to represent surface impedance models of generic liners and as it allows for an efficient numerical implementation. In particular, Dragna *et al.* [25] and Troian *et al.* [24] proposed the auxiliary differential equation (ADE) method, in which the calculation of the convolution is reduced to the time integration of additional first-order partial differential equations. This is especially well-suited for high-order methods. Recently, Shur *et al.* [26] extended this TDIBC based on the multipole model in the nonlinear regime.

The objectives of the paper are to propose and evaluate formulations of the TDIBC for the multipole model in the nonlinear regime and to exemplify sound propagation along a lined duct in high sound pressure environment. The impedance model proposed by Laly *et al.* [12] is used as the reference model for the perforated panel. Two approaches for the TDIBC in the nonlinear regime are considered. In the first one, based on Shur *et al.* [26], the impedance is interpolated as a function of the rms velocity in the orifice. In the second one, the poles and coefficients of the multipole model are directly interpolated as a function of the rms velocity in the orifice. The two approaches are validated against a one-dimensional (1D) impedance tube configuration, first for numerical experiments and then for measurements performed for three perforated plates. Application to a two-dimensional (2D) lined duct is then performed. The evolution of the liner attenuation with the excitation level is studied. The spatial variation of the surface impedance along the liner is analyzed. Finally, it is investigated whether or not accounting for the spatial variations of the impedance is important for accurately predicting the liner attenuation.

This paper is organized as follows. Section 2 presents the acoustic impedance model of Laly *et al.* [12] for predicting the response of perforated panels at high level of excitation. In Sec. 3, the numerical model that solves the linearized Euler equations in the time-domain using finite difference techniques is described. The time domain admittance boundary condition based on the multipole model is first presented in the linear regime. The two extensions of the TDABC in the

1  
2  
3  
4 nonlinear regime are then introduced. The validation of the proposed approach is performed in  
5  
6 Sec. 4. Application to a 2D lined duct is then investigated in Sec. 5. Concluding remarks are finally  
7  
8 given in Sec. 6.

## 9 10 11 **2. Impedance model of perforated plates in the nonlinear regime**

12  
13  
14 Throughout the paper, the time-dependence convention  $e^{-j\omega t}$  is used, where  $\omega$  denotes the an-  
15  
16 gular frequency,  $j$  the imaginary complex number ( $j^2 = -1$ ) and  $t$  the time. The air is characterized  
17  
18 by its density ( $\rho_0 = 1.211 \text{ kg m}^{-3}$ ), its dynamic viscosity ( $\eta = 1.84 \times 10^{-5} \text{ kg m}^{-1} \text{ s}^{-1}$ ) and the  
19  
20 corresponding sound speed ( $c_0 = 340 \text{ m s}^{-1}$ ). The geometry of the perforated plate is described by  
21  
22 its thickness  $h$ , the perforation radius  $r$  and the percentage open area (POA)  $\varphi$ .

23 Atalla and Sgard [13] modelled the perforated panel in the linear regime by an equivalent  
24  
25 fluid model following the Johnson-Allard approach [27]. The normalized acoustic impedance of a  
26  
27 perforated panel backed by an air cavity of depth  $D$  is

$$28 \quad Z_L = \frac{-j\omega\alpha_\infty h}{c_0\varphi} \left( 1 - \frac{\sigma\varphi}{j\omega\rho_0\alpha_\infty} \sqrt{1 - \frac{4j\omega\rho_0\eta\alpha_\infty^2}{\varphi^2\sigma^2\Lambda^2}} \right) - \coth(jk_0D), \quad (1)$$

29  
30  
31 where  $k_0 = \omega/c_0$  is the wave number in air. The parameters of the equivalent fluid are related  
32  
33 to the PP geometry. Thus, the viscous characteristic length  $\Lambda$  is equal to the perforation radius  
34  
35 ( $\Lambda = r$ ). The flow resistivity  $\sigma$  is given by  $\sigma = \frac{8\eta}{\varphi r^2}$  in the case of cylindrical orifices. The tortuosity  
36  
37  $\alpha_\infty$  is a function of the correction length  $\varepsilon$ , that accounts for sound radiation effects at the end of  
38  
39 the perforations through  $\alpha_\infty = 1 + \frac{2\varepsilon}{h}$ . The correction length is related to the POA and the radius  
40  
41 of perforation. Following Laly et al. [12], it can be written:

$$42 \quad \varepsilon = \Psi 0.48\sqrt{\pi r^2} \left[ \sum_{n=0}^8 a_n (\sqrt{\varphi})^n \right], \quad (2)$$

43  
44  
45 where  $0.48\sqrt{\pi r^2}$  is the correction length for a single circular orifice, the sum over the coefficients  
46  
47  $a_n$  is an approximation of the Fok function that accounts for orifice interaction effects [11] and  $\Psi$   
48  
49 is a constant. The coefficients  $a_n$  are given by  $a_0 = 1$ ,  $a_1 = -1.4092$ ,  $a_2 = 0$ ,  $a_3 = 0.33818$ ,  $a_4 = 0$ ,  
50  
51  $a_5 = 0.06793$ ,  $a_6 = -0.02287$ ,  $a_7 = 0.003015$  and  $a_8 = -0.01614$  [11] and  $\Psi$  is set to  $4/3$ . Note that  
52  
53 the Fok function and the empirical constant  $\Psi$  are not present in the original model proposed by  
54  
55 Atalla and Sgard [13], but are introduced here for coherence with the nonlinear model.

56  
57  
58 Laly et al. [12] proposed an extension of the model in Eq. (1) to characterize the acoustic  
59  
60 response of perforated plates in the nonlinear regime. The impedance model of a PP backed by an  
61  
62

air layer has the same form as in the linear regime:

$$Z_{\text{NL}} = \frac{-j\omega h}{c_0\varphi}\alpha_{\infty\text{NL}} \left( 1 - \frac{\sigma_{\text{NL}}\varphi}{j\omega\rho_0\alpha_{\infty\text{NL}}} \sqrt{1 - \frac{4j\omega\rho_0\eta\alpha_{\infty\text{NL}}^2}{\varphi^2\sigma_{\text{NL}}^2\Lambda^2}} \right) - \coth(jk_0D), \quad (3)$$

except that the flow resistivity  $\sigma_{\text{NL}}$  and the tortuosity  $\alpha_{\infty\text{NL}}$  now depend on the rms velocity in the orifice  $v_{\text{rms}}$ . The flow resistivity of the PP in the nonlinear regime is modelled via a Forchheimer-type law. It is thus equal to its value in the linear regime plus a nonlinear correction:

$$\sigma_{\text{NL}} = \sigma + \frac{\beta\rho_0(1-\varphi^2)}{\pi h\varphi C_D^2} \sqrt{2}v_{\text{rms}}, \quad (4)$$

where  $C_D$  is the discharge coefficient, that depends on the perforation geometry, the edge sharpness among others and that vary between 0.6 and 0.8 and  $\beta$  is a coefficient. Thereafter, the values used in Laly et al. [12], i.e.  $C_D = 0.76$  and  $\beta = 1.6$ , are employed. The tortuosity  $\alpha_{\infty\text{NL}}$  in the nonlinear regime is defined as in the linear regime by

$$\alpha_{\infty\text{NL}} = 1 + \frac{2\varepsilon_{\text{NL}}}{h}. \quad (5)$$

Following Maa [5], the correction length  $\varepsilon_{\text{NL}}$  is modified to account for the nonlinear effects with

$$\varepsilon_{\text{NL}} = \varepsilon \left( 1 + \frac{\sqrt{2}v_{\text{rms}}}{\varphi c_0} \right)^{-1}. \quad (6)$$

The tortuosity thus decreases with the increase of the acoustic velocity in the perforation.

The model proposed by Laly et al. [12] is more accurate for micro-perforated liners ( $r \leq 0.5$  mm) than for macro-perforated liners and for a POA range from 1 % to 5 % [28].

In this work, results are exemplified for three PP absorbers, whose photo is shown in Fig. 1. Their geometrical characteristics are given in Table 1. The PPs #1 and #2 correspond to micro-perforated plates, with perforation radius below 0.5 mm and POA in the order of 1%. PP#3 has a larger perforation radius and is in between a micro- and macro-perforated plate.

	PP#1	PP#2	PP#3
Plate thickness (mm)	1	1	1
Perforation radius (mm)	0.25	0.25	1
Perforation ratio (%)	1.5	1	1.5

Table 1: Geometric parameters of the PPs absorber.

1  
2  
3  
4  
5  
6  
7  
8  
9  
10  
11  
12  
13  
14  
15  
16  
17  
18  
19  
20  
21  
22  
23  
24  
25  
26  
27  
28  
29  
30  
31  
32  
33  
34  
35  
36  
37  
38  
39  
40  
41  
42  
43  
44  
45  
46  
47  
48  
49  
50  
51  
52  
53  
54  
55  
56  
57  
58  
59  
60  
61  
62  
63  
64  
65

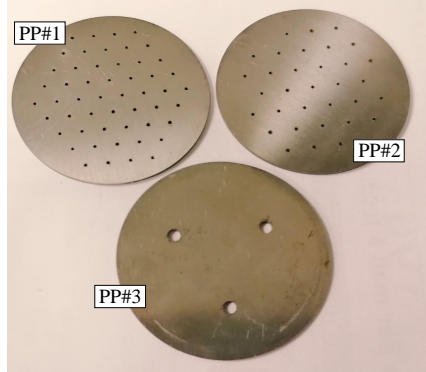


Figure 1: Photo of the three perforated plates considered.

### 114 3. Time-domain numerical model

#### 115 3.1. Geometrical configuration

116 An impedance tube, schematized in Fig. 2, is considered as a canonical problem to evaluate time-  
 117 domain impedance boundary conditions in the nonlinear regime. It is treated as a one-dimensional  
 118 problem. Denoting by  $x$  the spatial variable, the domain of interest is limited to  $0 \leq x \leq L$ . The  
 119 PP liner is located at  $x = L$  and an incident wave  $p_i(t)$  is travelling towards the liner.

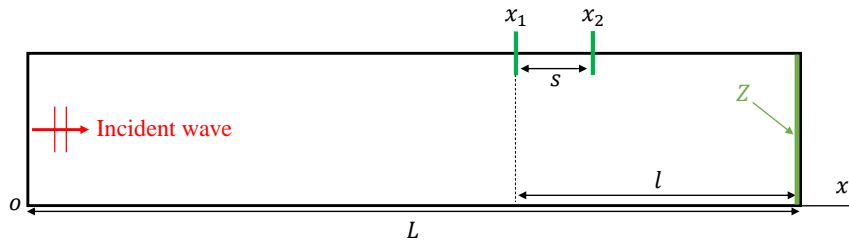


Figure 2: Schematic for the one-dimensional configuration, corresponding to an impedance tube.

#### 120 3.2. Equations and numerical methods

121 For acoustic perturbations of sufficiently small amplitude, sound propagation is governed by  
 122 the linearized Euler equations (LEE). For a homogeneous medium at rest, they write:

$$\begin{cases} \frac{\partial u}{\partial t} + \frac{1}{\rho_0} \frac{\partial p}{\partial x} = 0 \\ \frac{\partial p}{\partial t} + \rho_0 c_0^2 \frac{\partial u}{\partial x} = 0, \end{cases} \quad (7)$$

1  
2  
3  
4  
5  
6  
7  
8  
9  
10  
11  
12  
13  
14  
15  
16  
17  
18  
19  
20  
21  
22  
23  
24  
25  
26  
27  
28  
29  
30  
31  
32  
33  
34  
35  
36  
37  
38  
39  
40  
41  
42  
43  
44  
45  
46  
47  
48  
49  
50  
51  
52  
53  
54  
55  
56  
57  
58  
59  
60  
61  
62  
63  
64  
65

123 where  $u$  and  $p$  are the acoustic velocity and pressure, respectively.

124 The LEE are solved using high-order finite-difference time-domain methods. The spatial deriva-  
125 tives are calculated using optimized 4th-order finite differences schemes over 11 points [29, 30]. Time  
126 integration is performed using an optimized 6-stage 4th-order Runge-Kutta algorithm [31]. In order  
127 to avoid numerical instabilities and to remove grid-to-grid oscillations, optimized selective filters  
128 [30, 32] are applied after each time iteration.

129 The incident wave  $p_i(t)$  is prescribed using the method of characteristics. The incoming and  
130 outgoing characteristics in the computational domain at the boundary  $x = 0$ , denoted by  $q_i$  and  
131  $q_o$ , respectively, are given by:

$$q_i(t) = \frac{1}{2}(p(x = 0, t) + Z_0 u(x = 0, t)) \quad q_o(t) = \frac{1}{2}(p(x = 0, t) - Z_0 u(x = 0, t)), \quad (8)$$

132 with  $Z_0 = \rho_0 c_0$ . To force the incident wave and avoid reflections at the boundary, the method  
133 consists in determining the outgoing characteristic from the numerical solution and imposing the  
134 incoming characteristic to  $q_i(t) = p_i(t)$ , after each stage of the Runge-Kutta algorithm. The  
135 pressure and the velocity at the boundary are then corrected with the relations:

$$p(x = 0, t) = q_i(t) + q_o(t) \quad u(x = 0, t) = \frac{q_i(t) - q_o(t)}{Z_0} \quad (9)$$

136 Finally, all variables are initialized to zero at time  $t = 0$ .

### 137 3.3. Time-domain admittance boundary condition (TDABC) in the linear regime

138 Before discussing its extension for the nonlinear regime, the time-domain admittance boundary  
139 condition proposed by Troian et al. [24] for the linear regime is briefly summarized. Implementation  
140 on the admittance rather than on the impedance was preferred, as numerical instabilities were  
141 observed for some liners in the latter case. Note that implementations based on the reflection  
142 coefficient have been also proposed [19] and seem to offer better stability properties [33]. Denoting  
143 by  $Y(\omega)$  the normalized surface admittance, the admittance boundary condition is defined in the  
144 frequency domain by  $Z_0 U_n(\omega) = Y(\omega) P(\omega)$ , with  $U_n = \mathbf{U} \cdot \mathbf{n}$  where  $P(\omega)$  and  $\mathbf{U}(\omega)$  are the Fourier  
145 transforms of the acoustic pressure and velocity on the PP surface, respectively, and  $\mathbf{n}$  is the normal  
146 unit vector pointing into the liner surface.

147 The time domain admittance boundary condition (TDABC) is obtained from the translation of  
148 the frequency domain boundary condition, yielding the convolution  $Z_0 u_n(t) = [y * p](t)$ , where  $y(t)$   
149 is the surface admittance in the time domain. To avoid the tedious calculation of the convolution

1  
2  
3  
4 150 integral, Troian et al. [24] proposed to express the broadband admittance model  $Y(\omega)$  as a multipole  
5  
6 151 model:

$$7 \quad Y(\omega) = Y_\infty + \sum_{k=1}^P \frac{A_k}{\lambda_k - j\omega}, \quad (10)$$

8  
9  
10 152 where  $\lambda_k$  are the poles of the admittance and  $P$  denotes their number. Note that the poles and the  
11  
12 153 associated coefficients  $A_k$  are either real or come as complex conjugate pairs. Finally, the coefficient  
13  
14 154  $Y_\infty$  is real-valued.

15  
16 155 The analytical surface admittance of the PP is obtained from Eq. (1) with  $Y(\omega) = [Z_L(\omega)]^{-1}$   
17  
18 156 and is approximated by a multipole model in the form of Eq. (10). To do so, the poles and the  
19  
20 157 coefficients of the broadband admittance are determined using the vector fitting (VF) algorithm [34]  
21  
22 158 in the frequency band of interest. The VF algorithm allows the multipole model to have stable  
23  
24 159 poles. The passivity of the multipole model ( $\text{Re}[Y(\omega)] \geq 0$  for  $\omega > 0$ ) is however not guaranteed and  
25  
26 160 has to be checked for all frequencies and for each set of coefficients obtained with the VF algorithm.  
27  
28 161 In particular, it was observed that the real part of the multipole model can be negative at very  
29  
30 162 low frequencies for PP liners. Generally, this issue can be **overcome** by increasing the number of  
31  
32 163 poles. This solution might however not be worthwhile because we usually want to keep the number  
33  
34 164 of poles as small as possible to reduce the computational cost. As the minimum of  $\text{Re}[Y]$  denoted  
35  
36 165 by  $Y_-$  generally remains small ( $Y_-$  in the order of  $-10^{-3}$ ), an alternative to enforce passivity is to  
37  
38 166 add  $-Y_-$  to  $Y_\infty$  so that  $\text{Re}[Y] \geq 0$  over the frequency band of interest.

39  
40 167 With the multipole form, the surface admittance in the time domain has a closed-form expres-  
41  
42 168 sion, that greatly simplifies the expression of the convolution. After some calculation detailed in  
43  
44 169 Ref. [24], the time-domain admittance boundary condition (TDABC) finally relates the acoustic  
45  
46 170 velocity and pressure on the liner surface with the expression:

$$47 \quad Z_0 u_n(t) = Y_\infty p(t) + \sum_{k=1}^P A_k \phi_k(t), \quad (11)$$

48  
49 171 where the new temporal functions  $\phi_k(t)$ , called accumulator in Reymen et al. [22], verify the system  
50  
51 172 of ordinary differential equations (ODE):

$$52 \quad \frac{d\phi_k}{dt} + \lambda_k \phi_k(t) = p(t) \quad (12)$$

53  
54  
55  
56 173 This system is numerically solved using **the same time scheme as** for the LEE presented in Eq. (7).  
57  
58 174 Equations (11) and (12) constitute the TDABC.

59  
60 175 Note that the formulation of the TDABC presented in this section is an alternative to that  
61  
62  
63  
64  
65

1  
2  
3  
4 176 proposed in Ref. [24], as there is no explicit distinction between the real poles and the pairs of  
5  
6 177 complex conjugate poles. As a consequence, the accumulators  $\phi_k$  are complex-valued.  
7  
8

9 178 *3.4. Extension of the TDABC in the nonlinear regime*

10  
11 179 Some remarks are first made on nonlinear impedance models. Surface impedance is rigorously  
12  
13 180 defined in the linear regime. For a harmonic excitation, a surface impedance that depends on the  
14  
15 181 excitation amplitude seems relevant, as long as the harmonic distortion is negligible. For other types  
16  
17 182 of excitation, the concept of nonlinear surface impedance is somewhat empirical. A straightforward  
18  
19 183 extension of the impedance model proposed by Laly et al. [12] for broadband stationary signal is  
20  
21 184 to consider that the main information on the velocity in the perforations governing the nonlinear  
22  
23 185 effects remains its overall amplitude rather than any specific frequency-dependent information.  
24  
25 186 **Such approach has been employed by Eversman [15] for propagation of multiple tones inside a**  
26  
27 187 **lined duct using a frequency-domain finite element method.** Therefore, the impedance model in  
28  
29 188 Eq. (3) can be used as is for a broadband stationary excitation.<sup>1</sup> Despite its simplicity, recent  
30  
31 189 comparisons [35] have shown an excellent agreement between predictions using this approach and  
32  
33 190 measurements with an impedance tube for a white noise excitation.

34  
35 191 The rest of the study is thus limited to stationary signals. For non-stationary signals, such  
36  
37 192 as transient signals, other models than frequency-based surface impedance models might be bet-  
38  
39 193 ter suited to represent the acoustic response of perforated plates in the nonlinear regime. Thus,  
40  
41 194 Cummings [14] propose nonlinear differential equations in the time-domain, that directly relate the  
42  
43 195 velocity in the perforation and the pressure jump through the perforated plate. These equations are  
44  
45 196 obtained from simplification of the fluid mechanics equations and do not include all physical effects  
46  
47 197 considered in the surface impedance model, such as the effects of the interaction between holes  
48  
49 198 of the perforates on the end correction length or the reduction of the end correction length with  
50  
51 199 the increase of the orifice velocity. Comparisons were however performed for a transmitted pulse  
52  
53 200 through a perforated plate between measurements in an impedance tube and numerical predictions  
54  
55 201 and were promising. Implementation of such nonlinear models of perforated plates for time-domain  
56  
57 202 simulations in a lined duct has been done in Monteghetti *et al.* [33].

58  
59 203 The implementation of the nonlinear TDABC in the time-domain numerical model is now

---

60  
61  
62  
63  
64  
65  
<sup>1</sup>Other nonlinear surface impedance models are based on the rms acoustic pressure on the liner rather than the rms velocity in the perforations, as considered by Shur et al. [26]. The numerical methods presented subsequently can be also employed similarly.

1  
2  
3  
4 204 presented. It is based on the recent work of Shur et al. [26] that has extended the TDABC of  
5  
6 205 Troian et al. [24] in the nonlinear regime. To do so, a quasi-steady approach is employed. The  
7  
8 206 idea is that the rms velocity on the liner has to be determined from the numerical solution. As  
9  
10 207 the solution is however advanced in time starting from some initial conditions, a transient period  
11  
12 208 is necessarily present. Thus, a time-varying evaluation of  $v_{\text{rms}}$ , denoted by  $\tilde{v}_{\text{rms}}(t)$ , is determined  
13  
14 209 and the surface admittance is dynamically modified to  $Y(\omega, \tilde{v}_{\text{rms}})$ , until steady-state is reached.

15 210 Second, to account for the variation of the admittance with both  $\omega$  and  $v_{\text{rms}}$ , two approaches are  
16  
17 211 investigated. They are both based on the approximation of the admittance by a multipole model  
18  
19 212 for some reference values of  $v_{\text{rms}}$ , that allows for the use of the ADE method. In the first approach  
20  
21 213 proposed by Shur et al. [26], the admittance is determined for a given  $v_{\text{rms}}$  by interpolation. This  
22  
23 214 method was shown to be accurate and efficient. One of its drawback is that compared to the linear  
24  
25 215 regime, the number of poles significantly increases and is globally proportional to the number  
26  
27 216 of reference values of  $v_{\text{rms}}$  chosen for the interpolation. This first approach, referred to as the  
28  
29 217 interpolation of the admittance (IA) method is detailed in Sec. 3.4.1. We propose a second approach,  
30  
31 218 in which, the multipole coefficients, rather than directly the admittance, are calculated for a given  
32  
33 219  $v_{\text{rms}}$  by interpolation. Once the coefficients are known, the admittance is easily deduced. This  
34  
35 220 approach, referred to as the interpolation of the admittance parameters (IAP) method is presented  
36  
37 221 in Sec. 3.4.2.

### 38 222 *3.4.1. Interpolation of the admittance (IA)*

39 223 The method based on the interpolation of the admittance is first presented. Following Shur  
40  
41 224 et al. [26], we define a set of reference values for the rms velocity  $v_{\text{rms}}^{(l)}$ ,  $l = 1, 2, \dots, N$ . This set  
42  
43 225 covers the expected range of variation of  $v_{\text{rms}}$  and has to be adapted according to the problem  
44  
45 226 under consideration. At each of these reference values  $v_{\text{rms}}^{(l)}$ , the frequency-dependent admittance  
46  
47 227  $Y(\omega, v_{\text{rms}}^{(l)}) = [Z_{\text{NL}}(\omega, v_{\text{rms}}^{(l)})]^{-1}$  (see Eq. (3)) is approximated by a multipole model

$$48 \quad 49 \quad 50 \quad 51 \quad 52 \quad Y^{(l)}(\omega) = Y(\omega, v_{\text{rms}}^{(l)}) = Y_{\infty}^{(l)} + \sum_{k=1}^{P^{(l)}} \frac{A_k^{(l)}}{\lambda_k^{(l)} - j\omega}, \quad (13)$$

53 228 where the same notation than in Eq. (10) is employed. The poles and coefficients of the admittances  
54  
55 229 ( $Y_{\infty}^{(l)}$ ,  $A_k^{(l)}$  and  $\lambda_k^{(l)}$ ) are determined for the reference values  $v_{\text{rms}}^{(l)}$  using the VF algorithm. Note that  
56  
57 230 the number of real poles and pairs of complex conjugate poles can vary depending on the rms  
58  
59 231 velocity. Then, for any  $v_{\text{rms}}$  value in the range  $[v_{\text{rms}}^{(1)}, v_{\text{rms}}^{(N)}]$ , the admittance of the perforated panel  
60  
61 232 ( $Y(\omega, v_{\text{rms}})$ ) is calculated using a linear combination of the individual admittances at each of these

reference values  $v_{\text{rms}}^{(l)}$

$$Y(\omega, v_{\text{rms}}) = \sum_{l=1}^N \sigma_l(v_{\text{rms}}) Y^{(l)}(\omega) \quad \sum_{l=1}^N \sigma_l = 1, \quad (14)$$

where  $\sigma_l$  are the weights, that provide information about the rms velocity in the perforation.

As done by Shur et al. [26], the weights are obtained by linear interpolation between the defined reference values  $v_{\text{rms}}^{(l)}$ . Thus, for  $v_{\text{rms}}$  belonging into the range  $v_{\text{rms}}^{(l-1)} \leq v_{\text{rms}} \leq v_{\text{rms}}^{(l)}$ , the weights are calculated as follows:

$$\begin{cases} \sigma_l = \frac{v_{\text{rms}} - v_{\text{rms}}^{(l-1)}}{v_{\text{rms}}^{(l)} - v_{\text{rms}}^{(l-1)}} \\ \sigma_{l-1} = 1 - \sigma_l \\ \sigma_k = 0 \text{ for } k < (l-1) \text{ and } k > l \end{cases} \quad (15)$$

In the case where  $v_{\text{rms}}$  is outside the range of the reference values ( $v_{\text{rms}} \leq v_{\text{rms}}^{(1)}$  or  $v_{\text{rms}} \geq v_{\text{rms}}^{(N)}$ ), the admittance is set to the admittance at the corresponding end value of the velocity range, i.e. all the weights are equal to zero, except the weight of the end value which is equal to 1. Note that the linear interpolation is not a requirement of the method and that higher-order interpolation could be used.

It remains to evaluate  $v_{\text{rms}}$  from the numerical solution. To do so, the rms velocity is estimated at a given time  $t$  with the relation

$$\tilde{v}_{\text{rms}}^2(t) = \frac{1}{t} \int_0^t v^2(t') dt', \quad (16)$$

where  $v(t)$  is the velocity fluctuation in the orifice. Due to the conservation of the acoustic flow rate, it is equal to the ratio of the acoustic normal velocity on the liner to the POA, i.e.  $v(t) = u_n(t)/\varphi$ . Taking the time derivative of the above equation leads to the differential equation:

$$\frac{d(t\tilde{v}_{\text{rms}}^2)}{dt} = \frac{u_n^2(t)}{\varphi^2}, \quad (17)$$

that is integrated in time with the time-marching scheme to obtain  $\tilde{v}_{\text{rms}}(t)$ . In practice, a simpler approach is employed. The value of  $\tilde{v}_{\text{rms}}$  at the time iteration  $n$  is calculated from its value at iteration  $n-1$  using the recursive expression:

$$\tilde{v}_{\text{rms}}^2(n\Delta t) = \left(1 - \frac{1}{n}\right) \tilde{v}_{\text{rms}}^2[(n-1)\Delta t] + \frac{1}{n} \frac{u_n^2(n\Delta t)}{\varphi^2}, \quad (18)$$

with  $\Delta t$  the time step. This expression can be obtained by integrating Eq. (17) between two consecutive time steps and by assuming that  $u_n$  is constant over a time step.

Therefore, the nonlinear extension of the TDABC in Eq. (11) with the IA method is rewritten as follows

$$Z_0 u_n(t) = \sum_{l=1}^N \sigma_l(\tilde{v}_{\text{rms}}) \left( Y_{\infty}^{(l)} p(t) + \sum_{k=1}^{P^{(l)}} A_k^{(l)} \phi_k^{(l)}(t) \right), \quad (19)$$

where the accumulators  $\phi_k(t)$  are obtained by integrating the ODE:

$$\frac{d\phi_k^{(l)}}{dt} + \lambda_k^{(l)} \phi_k^{(l)}(t) = p(t) \quad (20)$$

and  $\tilde{v}_{\text{rms}}$  by integrating Eq. (17).

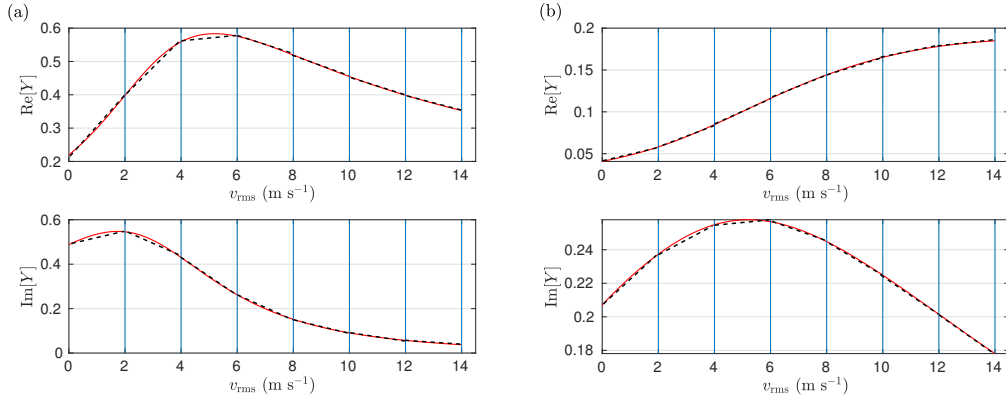


Figure 3: Real and imaginary parts of the admittance for a frequency of (a)  $f = 2000$  Hz and (b)  $f = 3000$  Hz as a function of the rms velocity in the perforation for PP#1 absorber with a cavity depth of 10 mm calculated with Eq. (3) (solid line) and by linear interpolation (dotted line). The vertical lines at  $v_{\text{rms}} = 0, 2, 4, 6, 8, 10, 12$  and  $14 \text{ m s}^{-1}$  show the reference values used for the interpolation.

In order to choose the set of reference values  $v_{\text{rms}}^{(l)}$ , the evolution of the admittance with the rms velocity in the perforation is investigated. Figure 3 shows the normalized admittance (solid line) as a function of  $v_{\text{rms}}$  for PP#1 with a cavity depth of 10 mm and for two frequencies (2000 and 3000 Hz). It is seen that the nonlinear behavior is strongly dependent on the frequency: the variation with  $v_{\text{rms}}$  is significant for 2000 Hz, which is close to the resonant frequency of the PP liner, but limited for 3000 Hz. In addition, the admittance is not varying simply with  $v_{\text{rms}}$ . In order to use linear interpolation, it is necessary to choose a sufficiently small step between two consecutive reference values to represent correctly the variations of  $Y$  with  $v_{\text{rms}}$ . The dotted line thus corresponds to a linear interpolation using a step of  $2 \text{ m s}^{-1}$ . With this step, the interpolated admittance shows a good agreement with the exact admittance.

Fig. 4 shows the comparison between the exact admittance model and its approximation with

the IA method for three rms velocities (4, 5, and 6 m s<sup>-1</sup>). This velocity range is chosen because the error in Fig. 3 is maximum in this range. Note that  $v_{\text{rms}} = 4$  and 6 m s<sup>-1</sup> are considered as reference values in the IA method: for these two rms velocities, the exact admittance is approximated by a multipole model using the VF algorithm. The approximation is performed for 200 Hz <  $f$  < 4000 Hz using two poles, which is seen to be sufficient to accurately represent the variation of  $Y$  over the entire frequency range of interest. For the intermediate rms velocity  $v_{\text{rms}} = 5$  m s<sup>-1</sup>, the admittance in the IA method is obtained by linear interpolation from the multipole models at  $v_{\text{rms}} = 4$  and 6 m s<sup>-1</sup>. Here also, a close agreement with the exact admittance is observed.

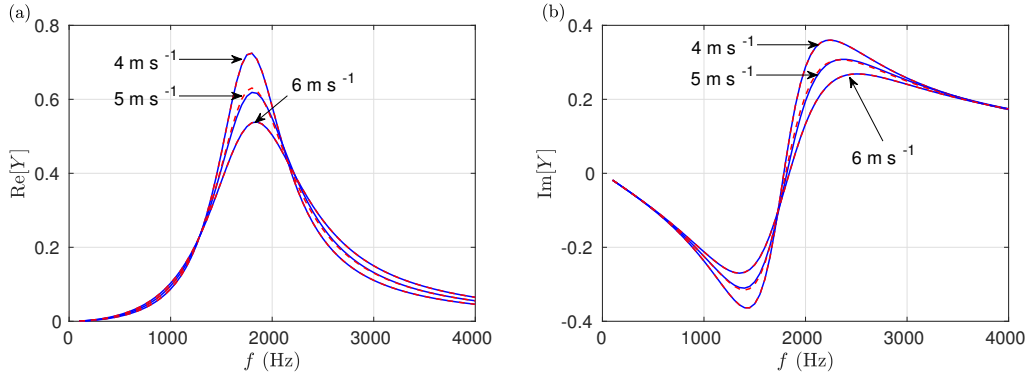


Figure 4: (a) Real and (b) imaginary parts of the admittance of PP#1 absorber with a cavity depth of 10 mm as a function of the frequency for three rms velocities: exact calculation (solid blue line) and approximation with the IA method (dotted red line).

In accordance with the discussion around Fig. 3, we have chosen the set of reference values for the rms velocity  $v_{\text{rms}}^{(l)} = 2, 4, 6, 8, 10$  and 12 m s<sup>-1</sup> with  $N = 6$ . For each reference value, the admittance is fitted over the frequency range 200 - 4000 Hz by a multipole model using the VF algorithm with two poles. The number of real poles and of pairs of complex conjugate poles for the reference values is indicated in Tab. 2 for the three PPs absorber. The related incident sound pressure levels (SPL) is also indicated. It represents the SPL of the incident wave, that generates the corresponding rms velocity in the perforation. It is estimated from the relation derived by Ingard [36] that expresses the rms incident pressure  $p_{i,\text{rms}}$  as a function of  $v_{\text{rms}}$ :

$$p_{i,\text{rms}} = \frac{\rho_0 c_0^2}{2} \frac{\varphi v_{\text{rms}}}{c_0} \left( 1 + \frac{1 - \varphi^2}{\varphi} \frac{\sqrt{2} v_{\text{rms}}}{c_0} \right) \quad (21)$$

This expression is valid only at the resonant frequency of the PP, for which the velocity in the perforation is maximum for a given incident SPL. To reach the same value of  $v_{\text{rms}}$  at frequencies

1  
2  
3  
4  
5  
6  
7  
8  
9  
10  
11  
12  
13  
14  
15  
16  
17  
18  
19  
20  
21  
22  
23  
24  
25  
26  
27  
28  
29  
30  
31  
32  
33  
34  
35  
286  
37  
38  
287  
39  
40  
288  
41  
289  
42  
43  
44  
290  
45  
291  
46  
47  
292  
48  
49  
293  
50  
294  
51  
52  
295  
53  
54  
296  
55  
56  
297  
57  
58  
298  
59  
60  
299  
61  
62  
63  
64  
65

**PP#1, PP#3**

Cavity depth (mm)		10						30					
Reference rms velocity ( $\text{m s}^{-1}$ )		2	4	6	8	10	12	2	4	6	8	10	12
Incident SPL (dB)		114	122	128	132	135	138	114	122	128	132	135	138
Poles number	real	0	0	0	0	0	0	0	0	0	0	0	0
	complex conjugate pair	1	1	1	1	1	1	1	1	1	1	1	1

**PP#2**

Cavity depth (mm)		10						30					
Reference rms velocity ( $\text{m s}^{-1}$ )		2	4	6	8	10	12	2	4	6	8	10	12
Incident SPL (dB)		112	121	127	131	134.5	137.5	112	121	127	131	134.5	137.5
Poles number	real	0	0	0	0	0	0	0	0	0	0	2	2
	complex conjugate pair	1	1	1	1	1	1	1	1	1	1	0	0

Table 2: Number of real poles and pairs of complex conjugate poles for the reference values  $v_{\text{rms}}^{(l)}$  and for the three PPs absorbers.

different from the resonant frequency, a larger incident SPL is necessary. Therefore, the SPL indicated in Tab. 2 has to be interpreted as the minimum incident SPL generating the corresponding value of the velocity in the perforation. For information, the poles and coefficients of the multipole model used for the IA method are indicated in Tab. A.4 in Appendix A for PP#1 with the cavity depths of 10 and 30 mm.

The main disadvantage of this method can be brought to light. For  $v_{\text{rms}}$  outside the range of the reference values, it is not possible to evaluate correctly the admittance. The range covered by the reference values has thus to be broadened considerably to avoid such cases. In addition, to represent accurately the variation of the admittance with  $v_{\text{rms}}$ , the step between two successive reference values should be sufficiently small. Therefore, the number of reference values and, hence, of poles can be significant with the IA method, which can lead to an increase in the computational cost. For PP liners, the admittance can be approximated over a broad range of frequencies using few poles: the cost of the IA method is thus moderate. For other types of liner, this can become a shortcoming of the IA method.

1  
2  
3  
4 300 *3.4.2. Interpolation of the admittance parameters (IAP)*  
5

6 301 In this section, a new approach to account for the nonlinear effects on the admittance is pro-  
7  
8 302 posed. To do so, the admittance is still written as a multipole model, as in Eq. (10), but the  
9  
10 303 coefficients and the poles are allowed to vary with  $v_{\text{rms}}$ . This gives:

$$11 \quad Y(\omega, v_{\text{rms}}) = Y_{\infty}(v_{\text{rms}}) + \sum_{k=1}^P \frac{A_k(v_{\text{rms}})}{\lambda_k(v_{\text{rms}}) - j\omega}. \quad (22)$$

12  
13  
14  
15 304 It is then necessary to calculate the poles and coefficients of the multipole model as a function  
16  
17 305 of  $v_{\text{rms}}$ . To do so, one idea could be to couple the VF algorithm and the time-domain numerical  
18  
19 306 model, so that the poles and the coefficients of the admittance are determined dynamically as the  
20  
21 307 value of  $\tilde{v}_{\text{rms}}$  changes. This would however require to run the VF algorithm after each iteration (or  
22  
23 308 after each step of the Runge-Kutta algorithm). Even if the VF algorithm usually takes few tenths  
24  
25 309 of a second to run, this would add complexity and computational cost to the approach. Especially  
26  
27 310 for multi-dimensional problems, it would be necessary to run the VF algorithm for each grid point  
28  
29 311 on the liner. A more efficient strategy is to have an approximate analytical expression giving the  
30  
31 312 evolution of the poles and coefficients of  $Y$  with  $v_{\text{rms}}$ . In this work, the multipole coefficients  
32  
33 313 (real and imaginary parts, separately) are approximated by a rational function with quadratic  
34  
35 314 polynomials. For example, one has:

$$36 \quad Y_{\infty}(v_{\text{rms}}) = \frac{Y_{\infty}^{n,0} + Y_{\infty}^{n,1} v_{\text{rms}} + Y_{\infty}^{n,2} v_{\text{rms}}^2}{1 + Y_{\infty}^{d,1} v_{\text{rms}} + Y_{\infty}^{d,2} v_{\text{rms}}^2}, \quad (23)$$

37  
38  
39 315 where  $Y_{\infty}^{n,0}$ ,  $Y_{\infty}^{n,1}$ ,  $Y_{\infty}^{n,2}$ ,  $Y_{\infty}^{d,1}$  and  $Y_{\infty}^{d,2}$  are constants. A similar expression holds for  $\text{Re}[A_k(v_{\text{rms}})]$ ,  
40  
41 316  $\text{Im}[A_k(v_{\text{rms}})]$ ,  $\text{Re}[\lambda_k(v_{\text{rms}})]$ , and  $\text{Im}[\lambda_k(v_{\text{rms}})]$ . The rational function approximation is determined  
42  
43 317 using the curve fitting toolbox of MATLAB (with data points obtained with the VF algorithm  
44  
45 318 for  $0 \leq v_{\text{rms}} \leq 12 \text{ m s}^{-1}$  with a step of  $1 \text{ m s}^{-1}$ ). Other approaches, such as the VF algorithm,  
46  
47 319 could also have been employed. As an example, the poles and coefficients of the multipole function  
48  
49 320 are plotted as a function of  $v_{\text{rms}}$  in Fig. 5 along with their rational function approximation for  
50  
51 321 PP#1 with a cavity depth of 10 mm. The constants of the rational function approximation for  
52  
53 322 the multipole coefficients are given in Appendix A in Tab. A.5 for PP#1 liner with the two cavity  
54  
55 323 depths of 10 and 30 mm.

56  
57 324 With the expression of the admittance in Eq. (22), the nonlinear extension of the TDABC in  
58  
59 325 Eq. (11) with the IAP method is defined as follows:

$$60 \quad Z_0 u_n(t) = Y_{\infty}(\tilde{v}_{\text{rms}}) p(t) + \sum_{k=1}^P A_k(\tilde{v}_{\text{rms}}) \phi_k(t), \quad (24)$$

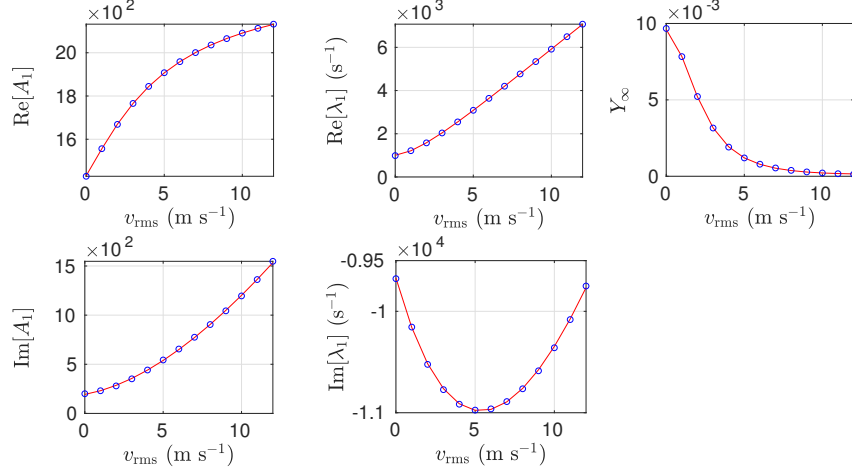


Figure 5: Coefficients of the multipole model as a function of the rms velocity  $v_{\text{rms}}$  (blue circle symbols) and their approximation (red solid lines) using a rational function (PP#1 for a cavity depth of 10 mm).

where the function  $\phi_k$  is governed by the ODE:

$$\frac{d\phi_k}{dt} + \lambda_k(\tilde{v}_{\text{rms}})\phi_k(t) = p(t) \quad (25)$$

and  $\tilde{v}_{\text{rms}}$  is determined from Eq. (17).

The IAP method is simpler to implement than the IA method. One difficulty is that, while in the VF algorithm, the total number of poles can be chosen, it is not possible to set their type (real poles or pair of complex conjugate poles). Therefore, a pair of complex conjugate poles can switch to two real poles for a given value of  $v_{\text{rms}}$  and inversely. Thus, the number of each type of poles is constant in all cases considered for rms velocities in the perforations between 0 and 12 m s<sup>-1</sup>, except for PP#2 with a cavity depth of 30 mm for which it changes from 10 m s<sup>-1</sup> (see Tab. 2). As a consequence, the variation of the poles and coefficients  $A_k$  and  $\lambda_k$  with  $v_{\text{rms}}$  is discontinuous when the poles type changes. A simple method to handle this issue with the IAP method is to define the poles and coefficients  $A_k$  and  $\lambda_k$  as piecewise rational functions of  $v_{\text{rms}}$  with a different set of coefficients for velocities for which the poles are real and for velocities for which the poles come as complex conjugate pairs. This approach has been tested for the impedance tube configuration, detailed in Sec. 4. It was shown to be effective but induced a longer transient before convergence. Results are not shown for conciseness. Because this issue was only noticed for PP#2 with a cavity depth of 30 mm and for a large velocity in the perforations, further investigation is left for future work.

## 4. 1D validation

The present section aims to verify that the proposed methods in Sec. 3.4 allow for an accurate representation of the surface impedance in the nonlinear regime. For that, the one-dimensional configuration corresponding to an impedance tube is considered, as shown in Fig. 2. Numerical experiments are first presented in Sec. 4.2 and comparisons to measurements are then performed in Sec. 4.3. The MATLAB codes employed for the numerical experiments with the IAP method are available in the supplementary material.

### 4.1. Numerical parameters

The computational domain ( $0 \leq x \leq L$ ) is discretized by 101 points with a uniform spatial step  $\Delta x = 0.0085$  m. The total simulation time is  $t_{\max} = 0.3$  s. The CFL (Courant-Fridrichs-Lewy) number is set to 0.5, which gives a time step  $\Delta t = 1.25 \times 10^{-5}$  s.

Numerical simulations are carried out for two types of incident waves, namely a harmonic and a broadband wave. For the former case, the incident wave is  $p_i(t) = \sqrt{2} p_{i,\text{rms}} \sin(2\pi ft)$ , where  $p_{i,\text{rms}}$  is the rms value. For the latter case, the incident wave is  $p_i(t) = p_{i,\text{rms}} s(t)$ , where  $s(t)$  is a broadband stationary signal of unitary rms value. The incident SPL is also used thereafter to characterize the excitation and is defined by:

$$\text{SPL}_i = 20 \log_{10} \left( \frac{p_{i,\text{rms}}}{p_{\text{ref}}} \right) \quad (26)$$

with the reference pressure set to  $p_{\text{ref}} = 2 \times 10^{-5}$  Pa.

The two-microphone method is employed to estimate the surface impedance of the PP liner ( $Z$ ) for both the numerical simulations and the experiments. The normalized surface impedance is determined from the frequency response function  $H_{12}$  between two microphones at positions  $x_1$  and  $x_2$

$$Z = -j \frac{\sin[k_0(l-s)] - H_{12} \sin(k_0 l)}{H_{12} \cos(k_0 l) - \cos[k_0(l-s)]}, \quad (27)$$

where  $l = L - x_1$  and  $s = |x_1 - x_2|$ . For the numerical simulations, the frequency response function  $H_{12}$  is obtained directly by the ratio of the Fourier transforms of the time pressure signals at positions  $x_1$  and  $x_2$ , in the case of harmonic excitation and by the ratio of the cross power spectral density of the time pressure signals at positions  $x_1$  and  $x_2$  to the power spectral density at  $x_2$ , in the case of broadband excitation.

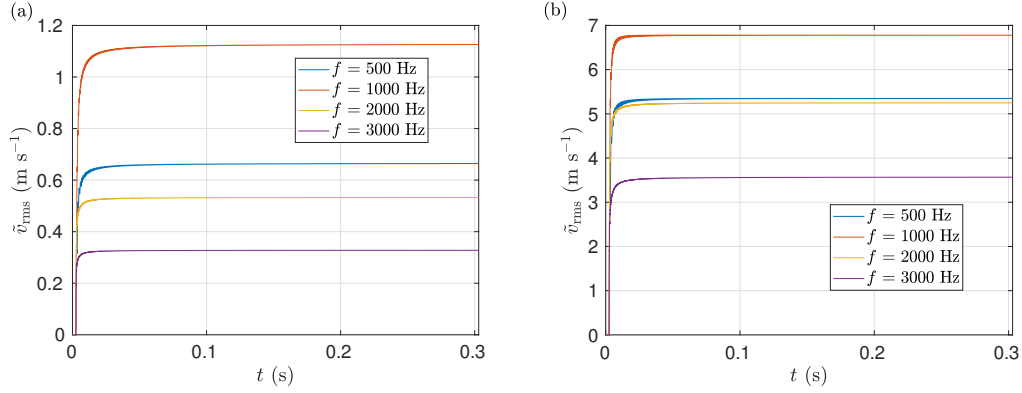


Figure 6: Time-variation of the estimated rms velocity in the perforation  $\tilde{v}_{\text{rms}}$  for PP#1 absorber with a cavity depth of 30 mm and for two incident SPL: (a)  $\text{SPL}_i = 110$  dB and (b)  $\text{SPL}_i = 130$  dB.

## 4.2. Numerical experiment

### 4.2.1. Harmonic excitation

The case of a harmonic excitation is first treated. Simulations are performed for incident waves with the same SPL and with frequencies between 200 and 4000 Hz, in steps of 100 Hz. At the initial time  $t = 0$ , all variables are set to zero, including  $\tilde{v}_{\text{rms}}$ . Once the incident wave impinges on the liner,  $\tilde{v}_{\text{rms}}$  increases. This modifies the surface impedance which in turn induces a variation of the acoustic field and of  $\tilde{v}_{\text{rms}}$ . This process repeats itself until a steady-state is obtained. This can be checked by looking at the convergence of  $\tilde{v}_{\text{rms}}$ , i.e. when the difference between the values of  $\tilde{v}_{\text{rms}}$  at two successive iterations becomes sufficiently small ( $\approx 10^{-3}$  m s $^{-1}$ ). Figure 6 shows the time-variation of the estimated rms velocity for four frequencies (500, 1000, 2000, 3000 Hz) at two incident SPL (110 and 130 dB) using PP#1. It is seen that  $\tilde{v}_{\text{rms}}$  monotonously increases with time and that convergence is reached from  $t = 0.2$  s for all cases. In addition, it can be noted that the rms velocity strongly depends on the frequency.

Figure 7 shows the rms velocity as a function of the frequency for PP#1 absorber for two cavity depths and for several incident SPL. The maximum of velocity is obtained near the resonant frequency and the latter is slightly shifted towards the high frequencies with the increase of the incident SPL. The variations of the rms velocity with the frequency for the two other absorbers PP#2 and PP#3 are similar but they are not shown for conciseness.

The real and imaginary parts of the admittance estimated from the numerical simulation with the IA and IAP methods are shown in Figs. 8 and 9 for PP#1 and PP#3 with two cavity depths and

1  
2  
3  
4  
5  
6  
7  
8  
9  
10  
11  
12  
13  
14  
15  
16  
17  
18  
19  
20  
21  
22  
23  
24  
25  
26  
27  
28  
29  
30  
31  
32  
33  
34  
35  
36  
37  
38  
39  
40  
41  
42  
43  
44  
45  
46  
47  
48  
49  
50  
51  
52  
53  
54  
55  
56  
57  
58  
59  
60  
61  
62  
63  
64  
65

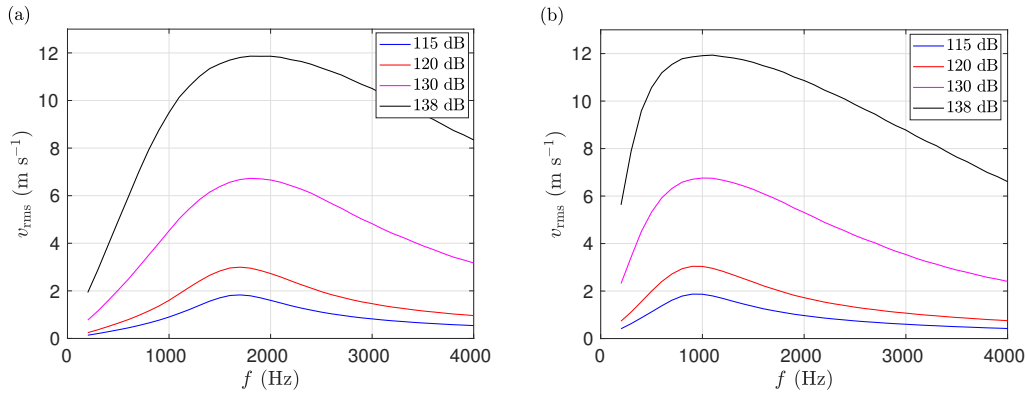


Figure 7: Variation of the rms velocity in the perforation with the frequency for several incident SPL and for PP#1 with two cavity depths: (a)  $D = 10$  mm and (b)  $D = 30$  mm.

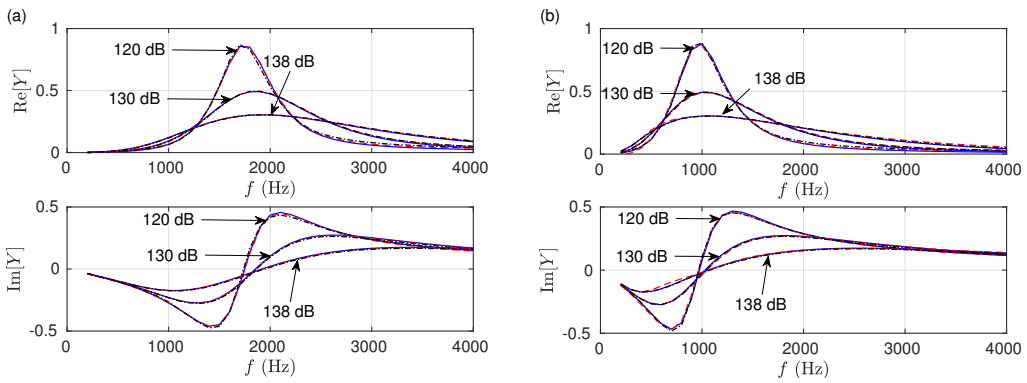


Figure 8: Admittance for PP#1 absorber with a cavity depth of (a)  $D = 10$  mm and (b)  $D = 30$  mm: calculated with the analytical model in Eq. (3) (blue solid) and determined from the numerical solution using the IAP (red dashed) and the IA (black dash-dotted) methods. A harmonic excitation is used.

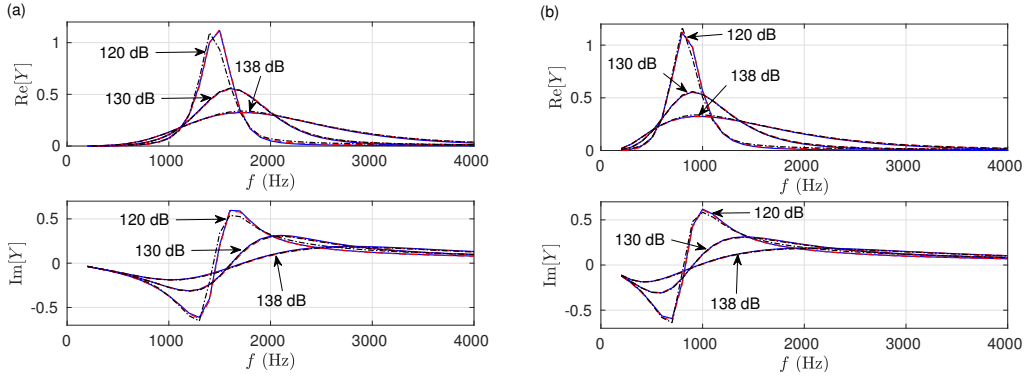


Figure 9: Admittance for PP#3 absorber with a cavity depth of (a)  $D = 10$  mm and (b)  $D = 30$  mm: calculated with the analytical model in Eq. (3) (blue solid) and determined from the numerical solution using the IAP (red dashed) and the IA (black dash-dotted) methods. A harmonic excitation is used.

for several incident SPL. It is seen that the surface admittance is significantly different depending on the incident SPL: in particular, increasing the incident SPL tends to flatten the curves. The corresponding analytical admittances calculated from Eq. (3) are also plotted in Figs. 8 and 9. Note that the rms velocity in the perforations determined from the numerical solution is used as input data for the analytical admittance model. For both IA and IAP methods, the numerical results are in good agreement with the analytical results over the entire frequency range for the reference values as well as for the intermediate values of the velocity. This shows that both methods allow for an accurate representation of the nonlinear admittance in the time domain.

#### 4.2.2. Broadband excitation

In this section, the case of a broadband excitation is studied. A white noise filtered using a Butterworth bandpass filter with lower and upper cutoff frequencies of 200 Hz and 4000 Hz, respectively, is employed.

The admittance determined from the numerical solution using the two methods IA and IAP is shown in Figs. 10 and 11 for PP#1 and #3 with two cavity depths and for three incident SPL. The dependence of the surface admittance in the nonlinear regime with the characteristics of the incident signal can be first noticed by comparing these two figures with Figs. 8 and 9. Indeed, the surface admittance for the harmonic excitation is significantly different from that for the broadband excitation, despite that the incident SPL on the liner is the same. In particular, for PP#3 (Figs. 9 and 11), the admittance amplitude for the broadband excitation is almost two times larger than for the harmonic excitation.

1  
2  
3  
4  
5  
6  
7  
8  
9  
10  
11  
12  
13  
14  
15  
16  
17  
18  
19  
20  
21  
22  
23  
24  
25  
26  
27  
28  
29  
30  
31  
32  
33  
34  
35  
36  
37  
38  
39  
40  
41  
42  
43  
44  
45  
46  
47  
48  
49  
50  
51  
52  
53  
54  
55  
56  
57  
58  
59  
60  
61  
62  
63  
64  
65

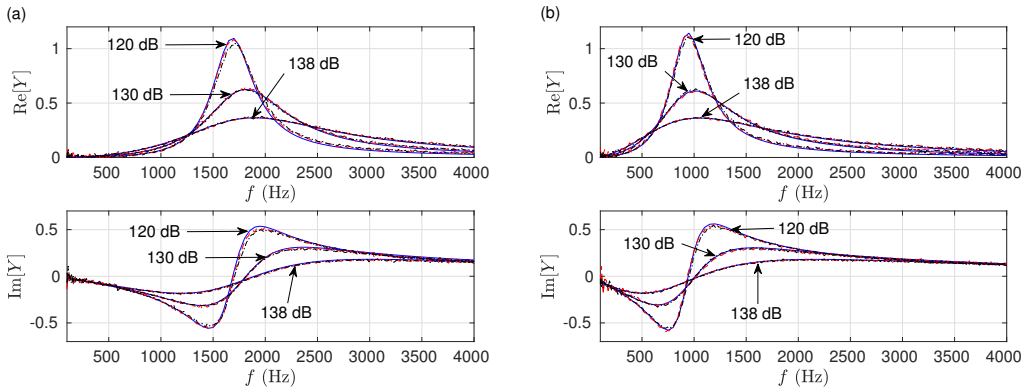


Figure 10: Admittance for PP#1 absorber with a cavity depth of (a)  $D = 10$  mm and (b)  $D = 30$  mm: calculated with the analytical model in Eq. (3) (blue solid) and determined from the numerical solution using the IAP (red dashed) and the IA (black dash-dotted) methods. A broadband excitation is used.

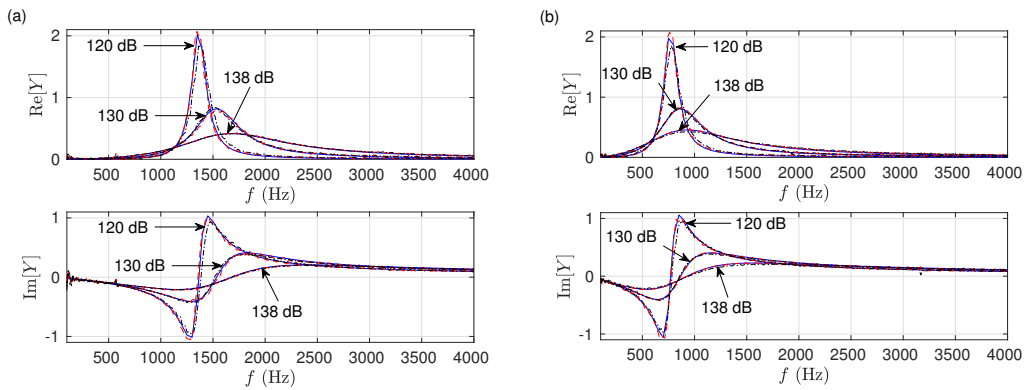


Figure 11: Admittance for PP#3 absorber with a cavity depth of (a)  $D = 10$  mm and (b)  $D = 30$  mm: calculated with the analytical model in Eq. (3) (blue solid) and determined from the numerical solution using the IAP (red dashed) and the IA (black dash-dotted) methods. A broadband excitation is used.

Second, the analytical admittance in Eq. (3) is also plotted in Figs. 10 and 11. Here as well, the rms velocity in the perforations deduced from the numerical simulation is used for the calculation of the analytical admittance. As a reminder,  $v_{\text{rms}}$  is a single value for the broadband admittance spectrum. As an example, for PP#1 absorber with a cavity depth of 10 mm,  $v_{\text{rms}}$  is equal to 1.8, 5 and 9.6  $\text{m s}^{-1}$  for incident SPL of 120, 130 and 138 dB, respectively. For the three incident sound pressure levels of 120, 130 and 138 dB, the predicted real and imaginary parts of the admittance are in good agreement with the analytical results for both PPs absorber with two cavity depths of 10 and 30 mm. The comparison is more favorable to the IAP method than to the IA method, which may be due to the low-order interpolation used in the IA method.

#### 4.3. Experimental validation

As a last check, numerical results with the nonlinear TDABC are compared to experimental results.

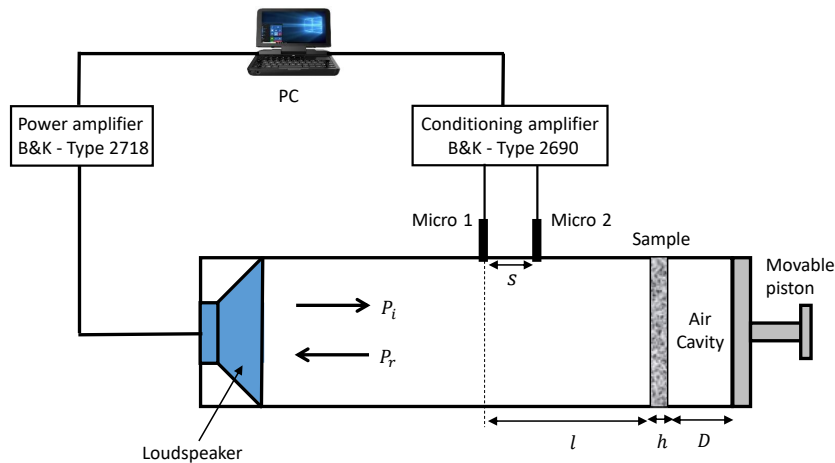


Figure 12: Schematic diagram of the impedance tube for measuring the surface admittance of a sample by using the two-microphone transfer-function method.

The measurements were performed using a B&K Type 4206 impedance tube kit, as illustrated in Fig. 12. The tube has a circular cross-section, with an inner diameter of 3 cm, yielding a cut-off frequency around 6400 Hz. The sample plate is located at the right hand side of the tube. An air cavity of depth  $D$  is created behind the plate by a movable piston which is used as a rigid backing wall. **Two sets of measurements were made, considering a harmonic excitation and a broadband excitation. For harmonic excitation, acoustic waves were generated by a loudspeaker mounted at**

the left hand side of the tube. For broadband excitation, the loudspeaker of the impedance tube kit was replaced by a JBL 2447H compression driver. The acoustic sources were powered by a B&K power amplifier type 2718. Pressure signals were measured using two flush-mounted 1/4" microphones (B&K type 4187), associated to two B&K type 2670 preamplifiers, a conditioning amplifier type 2690, and National Instrument 9250 front-end. An amplitude and phase calibration method was used to correct the transfer function between the two measurement channels.

The two-microphone method [37], as described in Sec. 4.1, was used to determine the surface impedance of the PP sample. The distance between the sample and the microphone 1 is  $l = 55$  mm and the two microphones were separated by a distance  $s = 20$  mm.

#### 4.3.1. Harmonic excitation

The measurements were carried out for the three PP absorbers described in Sec. 2 using a harmonic excitation over a frequency range between 500 and 4000 Hz in steps of 50 Hz. Two levels of excitation, corresponding to two different gains of the power amplifier, were considered. In the first case, denoted as the low SPL case, the amplifier gain was set to ensure that the SPL inside the tube was sufficiently small to be in the linear regime, while maintaining a good signal-to-noise ratio for all frequencies. In the second case, denoted as the high SPL case, the amplifier gain was increased to its maximum, while ensuring negligible harmonic distortion.

In the literature, measurements to characterize perforated plates at high SPL are rather performed by keeping the same level of the incident wave on the plate (see, e.g., Refs. [12, 38]), as done in the numerical experiments in Sec. 4.2.1. As we are mostly interested in validating the numerical model proposed in Sec. 3, this was not deemed necessary in this study.

A quantitative information on the acoustic excitation of the PP plate can be determined from the measurements. To do so, the acoustic pressure and velocity in the tube are expressed under the plane wave hypothesis as

$$P(x, \omega) = P_i(\omega)e^{jk_0x} + P_r(\omega)e^{-jk_0x} \quad U(x, \omega) = \frac{1}{Z_0} [P_i(\omega)e^{jk_0x} - P_r(\omega)e^{-jk_0x}] \quad (28)$$

where  $P_i$  and  $P_r$  represent the amplitude of the incident and reflected pressure waves in the tube, respectively. They can be determined thanks to the two-microphone method, with the relations:

$$P_i = jP(x_1) \frac{e^{-jk_0x_2} - H_{12} e^{-jk_0x_1}}{2 \sin(k_0s)} \quad P_r = -jP(x_1) \frac{e^{jk_0x_2} - H_{12} e^{jk_0x_1}}{2 \sin(k_0s)}. \quad (29)$$

Fig. 13 shows the amplitude of the incident wave  $|P_i|$  for PP#1 absorber with a cavity depth of 30 mm as a function of the driving frequency for the low and the high SPL cases. Although it can be

1  
2  
3  
4  
5  
6  
7  
8  
9  
10  
11  
12  
13  
14  
15  
16  
17  
18  
19  
20  
21  
22  
23  
24  
25  
26  
27  
28  
29  
30  
31  
32  
33  
34  
35  
36  
37  
38  
39  
40  
41  
42  
43  
44  
45  
46  
47  
48  
49  
50  
51  
52  
53  
54  
55  
56  
57  
58  
59  
60  
61  
62  
63  
64  
65

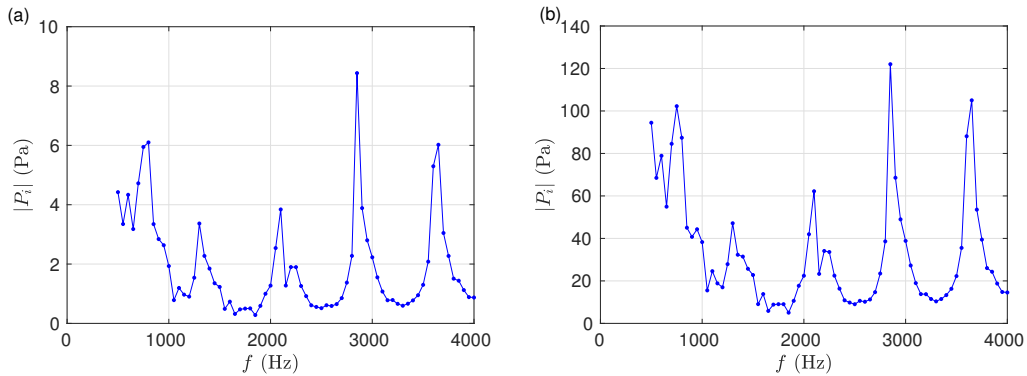


Figure 13: Measured amplitude of the incident acoustic pressure for PP#1 absorber with a cavity depth of 30 mm for (a) low and (b) high SPL cases.

455 expected that the amplitude of the acoustic wave generated by the loudspeaker is constant over the  
 456 entire frequency range, the amplitude of the incident wave greatly varies with the frequency. The  
 457 incident pressure is maximal for some frequencies; **this could be related** to the resonant frequencies  
 458 of the tube. For the low SPL case,  $|P_i|$  is below 9 Pa for all frequencies corresponding to incident  
 459 SPL below 110 dB. For the high SPL case,  $|P_i|$  reaches a maximum of 122 Pa for  $f = 2850$  Hz,  
 460 corresponding to an incident SPL of about 133 dB.

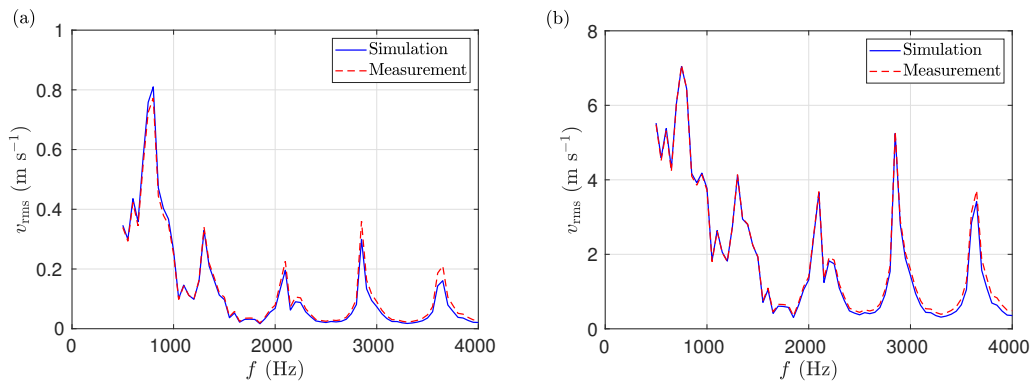


Figure 14: Rms amplitude of the velocity in the perforations for a harmonic excitation determined from the experiments and from the numerical simulation for PP#1 absorber with a cavity depth of 30 mm for the (a) low and (b) high SPL cases.

461 The numerical simulations are performed using the IAP method for the TDABC. In addition  
 462 to the nonlinear surface admittance model of the PP liner, the amplitude of the incident wave has  
 463 to be prescribed. It is set to the value determined in the experiments, i.e.  $p_{i,rms} = |P_i|/\sqrt{2}$ .

1  
2  
3  
4  
5  
6  
7  
8  
9  
10  
11  
12  
13  
14  
15  
16  
17  
18  
19  
20  
21  
22  
23  
24  
25  
26  
27  
28  
29  
30  
31  
32  
33  
34  
35  
36  
37  
38  
39  
40  
41  
42  
43  
44  
45  
46  
47  
48  
49  
50  
51  
52  
53  
54  
55  
56  
57  
58  
59  
60  
61  
62  
63  
64  
65

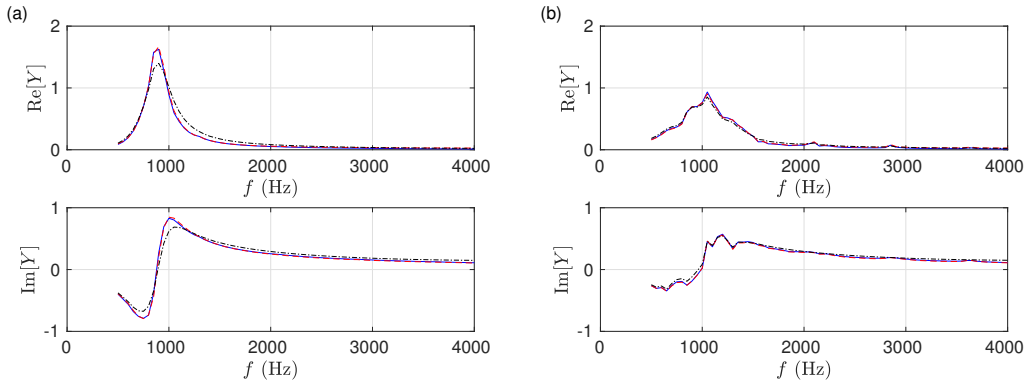


Figure 15: Surface admittance of PP#1 absorber with a cavity depth of 30 mm for a harmonic excitation for the (a) low and (b) high SPL cases: measured (black dash-dotted) and determined from the analytical model in Eq. (3) (blue solid) and from the numerical solution (red dashed).

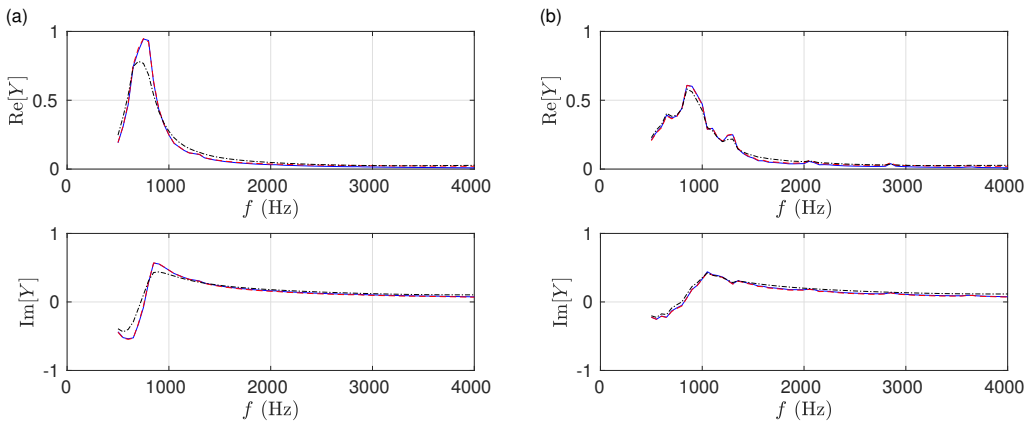


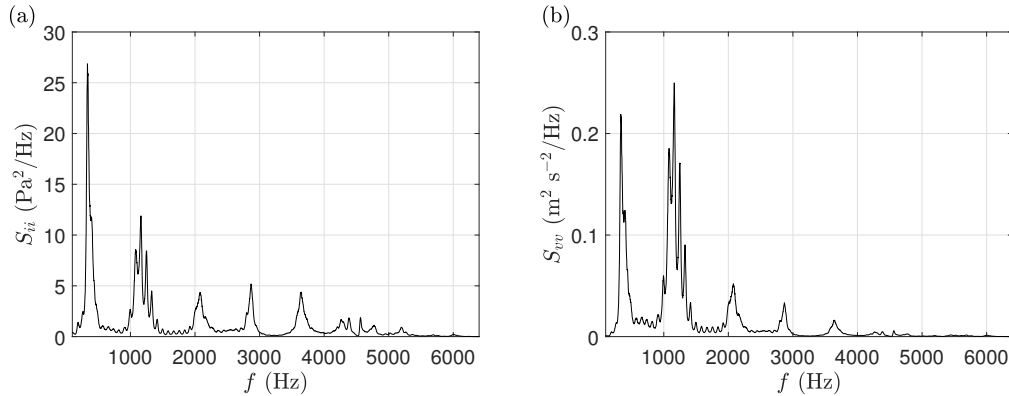
Figure 16: Surface admittance of PP#2 absorber with a cavity depth of 30 mm for a harmonic excitation for the (a) low and (b) high SPL cases: measured (black dash-dotted) and determined from the analytical model in Eq. (3) (blue solid) and from the numerical solution (red dashed).

464 The comparison between the experimental and numerical results is now presented. The rms  
465 amplitude of the velocity in the perforations is shown in Fig. 14 both for the experiments and for the  
466 numerical solution and for PP#1 with a cavity depth of 30 mm. Note that the experimental value  
467 of  $v_{\text{rms}}$  is determined from the pressure measurements with the two microphones using Eq. (28),  
468 which yields  $v_{\text{rms}} = |U(x = L)|/(\sqrt{2}\varphi)$ . An excellent agreement is seen at both low and high  
469 SPL. In addition, the frequency of the peaks observed in Fig. 14 is in accordance with those of the  
470 incident pressure amplitude in Fig. 13.

1  
2  
3  
4 471 The experimental admittances obtained for PP#1 and #2 are shown in Figs. 15 and 16, re-  
5  
6 472 spectively, along with those determined from the numerical models for the two levels of excitation.  
7  
8 473 Both are determined with the two-microphone method using Eq. (27). The analytical admittance  
9  
10 474 obtained with the Laly model using the rms velocity in the perforations determined from the  
11  
12 475 measurements is also plotted. A good agreement is obtained between the measurements and the  
13  
14 476 numerical and analytical models, especially for the high SPL case. We can also note the difference  
15  
16 477 in the real and imaginary parts of the admittance between the low and the high SPL cases, due to  
17  
18 478 the nonlinear effect. In addition, the abrupt variations of the surface admittance observed for the  
19  
20 479 high SPL case are due to the corresponding variations of the incident pressure with the frequency.

#### 21 480 4.3.2. *Broadband excitation*

22  
23 481 The measurements were repeated for the three PPs absorbers using a white noise signal as  
24  
25 482 the excitation signal and for several levels of excitation. Results are exemplified below for PP#1  
26  
27 483 absorber with a cavity depth of 30 mm. The comparisons for PP#2 and PP#3 both with a cavity  
28  
29 484 depth of 30 mm are shown in Appendix B.



30  
31  
32  
33  
34  
35  
36  
37  
38  
39  
40  
41  
42  
43  
44  
45  
46  
47 Figure 17: One-sided power spectral densities of (a) the incident pressure and (b) the velocity in the perforations for  
48  
49 PP#1 absorber with a cavity depth of 30 mm. A broadband excitation is used.

50  
51 485 Information on the incident pressure has to be obtained from the experiments for the numerical  
52  
53 486 simulations. With this aim, the power spectral density of the incident pressure  $S_{ii}$  is calculated  
54  
55 487 from those of the pressure at the two microphones based on Eq. (29). For comparison purpose,  
56  
57 488 the power spectral density of the velocity in the perforations  $S_{vv}$  is also calculated on the basis  
58  
59 489 of Eq. (28). Only the part of the spectra below the tube cutoff frequency, i.e. for  $f < 6400$  Hz,  
60  
61 490 is considered. The power spectral densities are shown in Fig. 17. The spectrum of the incident

491 pressure is not flat in the experiments, probably due to the resonances of the impedance tube, as  
 492 already noticed for the harmonic excitation in Sec. 4.3.1. This is also the case for the spectrum  
 493 of the velocity in the perforations. Note that the variations of  $S_{vv}$  with the frequency is slightly  
 494 different from that of  $S_{ii}$ . The rms values of the incident pressure and velocity in the perforations  
 495 are then estimated by integrating the corresponding power spectral density from 100 Hz up to  
 496 6400 Hz.

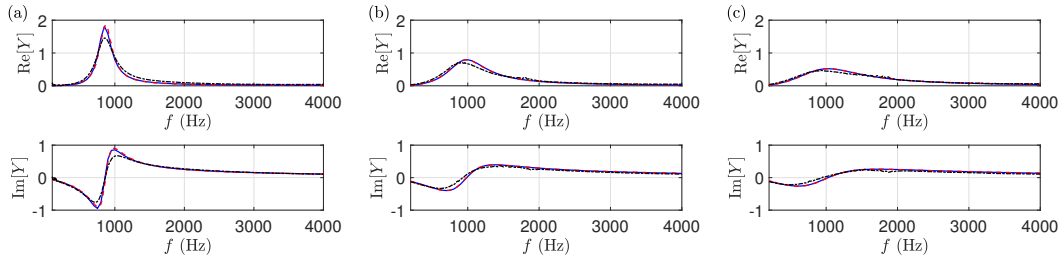


Figure 18: Surface admittance of PP#1 absorber with a cavity depth of 30 mm for a broadband excitation and for three incident SPL (a) 76.4 dB, (b) 126.4 dB and (c) 133.1 dB: measured (black dash-dotted) and determined from the analytical model in Eq. (3) (blue solid) and from the numerical solution (red dashed).

497 The numerical simulations are carried out using the IAP method for the TDABC. The incident  
 498 pressure signal is a random signal, built so that its power spectral density is equal to the one  
 499 measured. It induces in particular that the rms value of the incident pressure is the same in the  
 500 simulations and in the experiments.

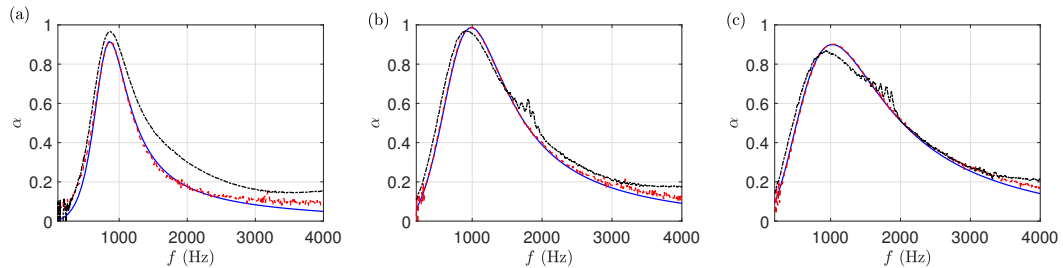


Figure 19: Absorption coefficient of PP#1 absorber with a cavity depth of 30 mm for a broadband excitation and for three incident SPL (a) 76.4 dB, (b) 126.4 dB and (c) 133.1 dB: measured (black dash-dotted) and determined from the analytical model in Eq. (3) (blue solid) and from the numerical solution (red dashed).

501 Fig. 18 shows the surface admittance determined from the measurements for three incident  
 502 SPL: 76.4 dB in (a), corresponding to the linear regime, and 126.4 dB and 133.1 dB in (b) and  
 503 (c), respectively, corresponding to the nonlinear regime. The variations of the surface admittance

with the incident SPL are similar to those observed in Sec. 4.2.2: the amplitude of the real and imaginary parts of  $Y$  decreases and the peak of  $\text{Re}[Y]$  widens with the increase of the incident SPL. The surface admittance deduced from the numerical simulations is also plotted in Fig. 18. While the match is not perfect with the measurements, a close agreement is noted. In particular, the evolution of the admittance with the incident SPL is well reproduced. Finally, the analytical model in Eq. (3) is also represented using the rms velocity in the perforations determined from the numerical simulations as input.

As an additional comparison, the corresponding absorption coefficients  $\alpha$  are plotted in Fig. 19 for the three incident SPL. The impact of the incident SPL on the measured absorption coefficient is noticeable: the absorption bandwidth broadens and the maximum of  $\alpha$  reduces with the increase of the incident SPL. Some ripples are seen in Figs. 19 (b) and (c) near 1800 Hz in the experimental curves; they are related to a lack of coherence due to low values of pressure at the microphones in this frequency range. The absorption coefficient determined from the numerical and analytical models are in good agreement with the measured one. While the curves of  $\alpha$  are not superimposed, the numerical simulations capture especially the evolution of the absorption coefficient with the increase of the incident SPL.

Finally, the rms amplitude of the velocity in the perforations deduced from the experiments and from the numerical simulations is reported in Tab. 3 for several incident SPL. It is observed that  $v_{\text{rms}}$  is noticeably well predicted from the numerical simulations.

Incident SPL (dB)		76.4	86.2	96.7	106.0	116.2	126.4	133.1
$v_{\text{rms}}$ (m s <sup>-1</sup> )	exp.	$1.24 \times 10^{-2}$	$3.69 \times 10^{-2}$	$1.21 \times 10^{-1}$	$3.56 \times 10^{-1}$	1.14	3.37	6.44
	num.	$1.49 \times 10^{-2}$	$4.86 \times 10^{-2}$	$1.60 \times 10^{-1}$	$4.54 \times 10^{-1}$	1.35	3.56	6.36

Table 3: Rms amplitude of the velocity in the perforations for PP#1 absorber with a cavity depth of 30 mm for a broadband excitation: values deduced from the experiments and from the numerical simulations.

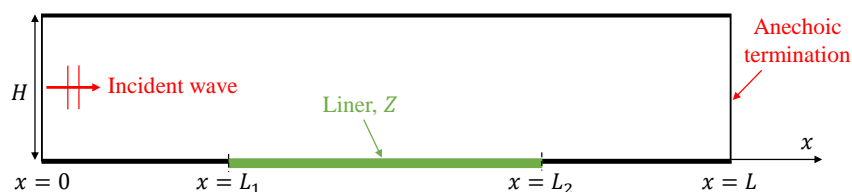
## 5. Application to a 2D lined duct

This section is concerned with a two-dimensional (2D) lined duct, which is representative of industrial applications. The objectives are to evaluate the numerical model including the nonlinear TDABC in this situation as well as to analyze the impact of nonlinear TDABC on sound propagation and attenuation in a 2D lined duct. In particular, the nonlinear admittance model of PP liners depends on the velocity in the perforations. It is expected that this quantity varies significantly

1  
2  
3  
4 529 along the treatment and, as a consequence, that it is also the case for the surface admittance.  
5  
6 530 Most of the existing methods for predicting sound propagation in a duct however consider a treat-  
7  
8 531 ment with a uniform admittance. It is therefore worthwhile to investigate whether accounting for  
9  
10 532 the spatial variations of the admittance at high excitation level is important for predicting the  
11  
12 533 transmission loss in a lined duct.

### 14 534 5.1. Numerical configuration

15  
16 535 A 2D lined duct of size  $L \times H = 0.812 \text{ m} \times 0.0508 \text{ m}$  is considered, as shown in Fig. 20. The liner  
17  
18 536 of length 0.406 m is located on the duct lower wall from  $x = L_1 = 0.203 \text{ m}$  to  $x = L_2 = 0.609 \text{ m}$ .  
19  
20 537 The other duct walls are rigid. This geometry corresponds to that of the Grazing Incidence Tube  
21  
22 538 of NASA (see, e.g., Ref. [39]), which is one of the well-known duct facility for evaluating liner  
23  
24 539 efficiency. There is no flow and the sound speed and air density are constant.



25  
26  
27  
28  
29  
30  
31  
32  
33  
34  
35  
36  
37  
38  
39  
40  
41  
42  
43  
44  
45  
46  
47  
48  
49  
50  
51  
52  
53  
54  
55  
56  
57  
58  
59  
60  
61  
62  
63  
64  
65

Figure 20: Schematic of the 2D lined duct.

540 All the results presented in this section are obtained for the PP#1 absorber with a cavity depth  
541 of 10 mm. The frequency range of interest is between 200 Hz and 3000 Hz, which respects the  
542 cut-off frequency (around 3.35 kHz) of the duct. Two types of incident pressure waveforms, i.e.  
543 harmonic and broadband, are considered. The broadband signal is obtained by filtering a white  
544 noise signal using a Butterworth bandpass filter with lower and upper cutoff frequencies set to  
545 200 Hz and 3000 Hz, respectively.

546 The 2D LEEs are solved using the numerical methods presented for the 1D case in Sec. 3.2.  
547 At the boundary  $x = 0$ , an incident plane wave propagating along the  $x$ -direction is generated  
548 using the method of characteristics, as described in Sec. 3.2. At  $x = L$ , a non-reflecting boundary  
549 condition is applied, using also the method of characteristics: the idea is the same, except that the  
550 incoming characteristic variable into the computational domain at the interface is set to zero so  
551 that no reflected waves are generated at the boundary. Finally, the normal velocity is set to zero  
552 on the duct rigid walls and the TDABC is applied along the lined section using the interpolation  
553 of the admittance parameters (IAP) approach presented in Sec. 3.4.2.

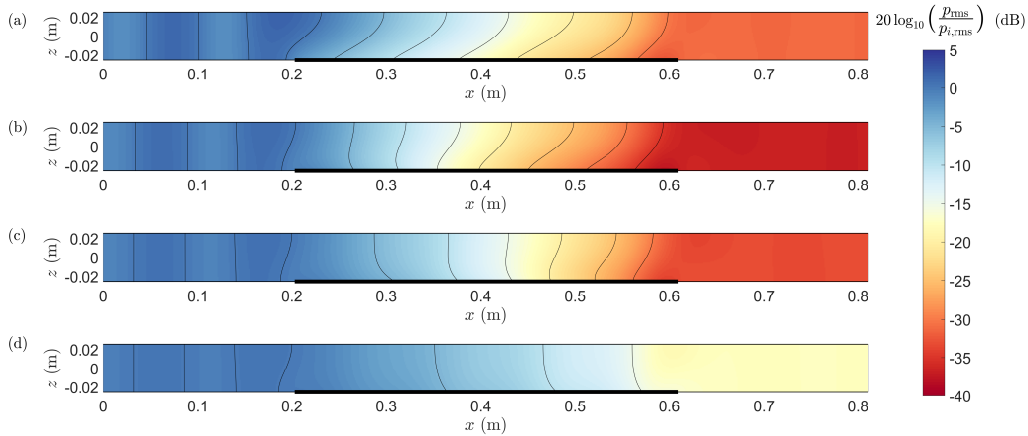
1  
2  
3  
4  
554 The mesh is uniform in the  $x$ -direction with a size  $\Delta x = 1.1 \times 10^{-3}$  m. Along the  $z$ -direction,  
6  
7  
8  
9  
10  
11  
12  
13  
14  
15  
16  
17  
18  
19  
20  
21  
22  
23  
24  
25  
26  
27  
28  
29  
30  
31  
32  
33  
34  
35  
36  
37  
38  
39  
40  
41  
42  
43  
44  
45  
46  
47  
48  
49  
50  
51  
52  
53  
54  
55  
56  
57  
58  
59  
60  
61  
62  
63  
64  
65

554 The mesh is uniform in the  $x$ -direction with a size  $\Delta x = 1.1 \times 10^{-3}$  m. Along the  $z$ -direction,  
555 the mesh size is progressively reduced towards the liner walls with a stretching factor of 0.99. It is  
556 equal to  $\Delta z = 1.1 \times 10^{-3}$  m at the duct axis and  $\Delta z = 8.19 \times 10^{-4}$  m on the walls. The time step  
557 is set to  $\Delta t = 2 \times 10^{-6}$  s, which yields a CFL number of 0.84. The total simulation time is 0.02 s  
558 for the harmonic excitation. It is increased to 0.35 s for the broadband excitation to get a longer  
559 signal in order to improve spectral resolution.

## 560 5.2. Harmonic excitation

### 561 5.2.1. Effect of the incident SPL

562 Results are first considered for several incident SPL and for a driving frequency of 1600 Hz,  
563 which is close to the resonant frequency of the liner. The contours of the SPL are depicted in Fig. 21  
564 for four incident SPL. The reference for the SPL calculation is chosen here as the rms amplitude of  
565 the incident wave to ease the comparison between the results. The SPL maps are globally similar  
566 in the rigid section for  $x < L_1$ . For the incident SPL of 120 and 130 dB, differences from the case  
567 of an incident SPL equal to 80 dB can already be seen. The isolines above the liner are noticeably  
568 modified, especially the slope on the liner. The SPL in the exit section ( $x > L_2$ ) also depends on  
569 the incident SPL. Finally, for the largest incident SPL of 140 dB, **strong alteration** of the SPL map  
570 is observed.



57  
58  
59  
60  
61  
62  
63  
64  
65

Figure 21: SPL ( $20 \log_{10}(p_{\text{rms}}/p_{i,\text{rms}})$ ) in dB for an incident SPL of: (a) 80 dB, (b) 120 dB, (c) 130 dB and (d) 140 dB with a harmonic excitation at  $f = 1600$  Hz. The liner location is indicated by the black thick horizontal line. Isolines are plotted every 5 dB in black lines.

1  
2  
3  
4  
5  
6  
7  
8  
9  
10  
11  
12  
13  
14  
15  
16  
17  
18  
19  
20  
21  
22  
23  
24  
25  
26  
27  
28  
29  
30  
31  
32  
33  
34  
35  
36  
37  
38  
39  
40  
41  
42  
43  
44  
45  
46  
47  
48  
49  
50  
51  
52  
53  
54  
55  
56  
57  
58  
59  
60  
61  
62  
63  
64  
65

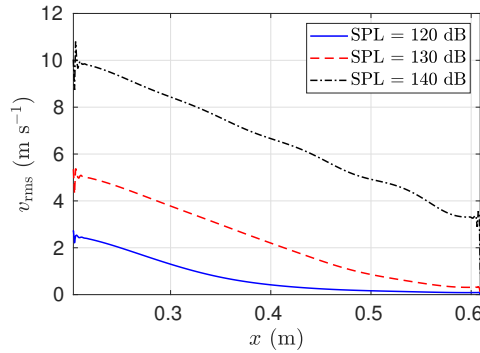


Figure 22: Variation along the liner of the rms velocity for three incident SPL of 120, 130 and 140 dB with a harmonic excitation at  $f = 1600$  Hz.

571 In order to analyze the evolution of the acoustic field with the incident SPL, the properties  
572 of the liner are investigated. Fig. 22 shows the variation of the rms velocity in the perforations  
573 along the liner for three incident SPL of 120, 130 and 140 dB. The effect of the liner is reflected by  
574 the reduction of  $v_{\text{rms}}$  along the liner. It decreases almost linearly for the incident SPL of 130 and  
575 140 dB. For 120 dB, it decreases also linearly at the beginning of the liner but less rapidly from  
576  $x = 0.4$  m.

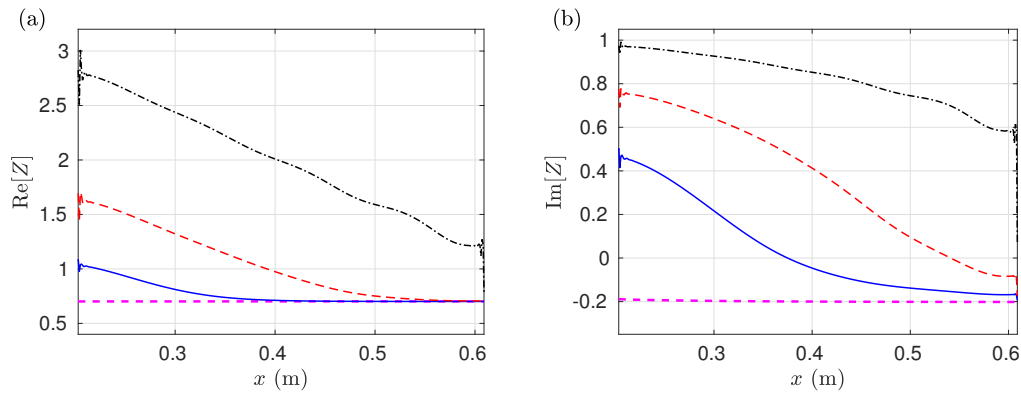


Figure 23: Variation along the liner of the real (a) and imaginary (b) parts of the impedance for four incident SPL of 80 dB (magenta dashed lines), 120 dB (blue solid lines), 130 dB (red dashed lines) and 140 dB (black dashed-dotted lines) with a harmonic excitation at  $f = 1600$  Hz.

577 The corresponding spatial variation of the surface impedance is depicted in Fig. 23 for four  
578 incident SPL. For the smallest incident SPL (80 dB), the real and imaginary parts of the impedance  
579 are constant along the liner and equal to the values in the linear regime. As the SPL increases,

1  
2  
3  
4  
5  
6  
7  
8  
9  
10  
11  
12  
13  
14  
15  
16  
17  
18  
19  
20  
21  
22  
23  
24  
25  
26  
27  
28  
29  
30  
31  
32  
33  
34  
35  
36  
37  
38  
39  
40  
41  
42  
43  
44  
45  
46  
47  
48  
49  
50  
51  
52  
53  
54  
55  
56  
57  
58  
59  
60  
61  
62  
63  
64  
65

large spatial variations of the impedance are noticed. In more details, the impedance is seen to vary at the beginning of the liner before reaching almost the impedance value in the linear regime. Thus, the resistance is almost equal to that in the linear regime from  $x = 0.4$  m for an incident SPL of 120 dB and from  $x = 0.55$  m for an incident SPL of 130 dB. For the largest SPL (140 dB), this is however not the case and the impedance remains different from that in the linear regime along the whole liner. The spatial variations of the impedance echo the recent studies of Lafont *et al.* [40] and Chen *et al.* [41], in which impedance eduction of PP liners in high SPL environments was performed from measurements or numerical simulations. In order to improve comparisons with the reference results, a spatially-varying impedance function (linear or piecewise linear) was used. This was also discussed in detail by Roncen *et al.* [16]. The authors proposed an iterative strategy based on a frequency-domain solver of the linearized Euler equations for two objectives: first, for prediction of the acoustic field in a duct lined with a perforate plane liner accounting for the spatial variations of the surface impedance and second, for eduction of a spatially-varying surface impedance at high excitation level from measurements.

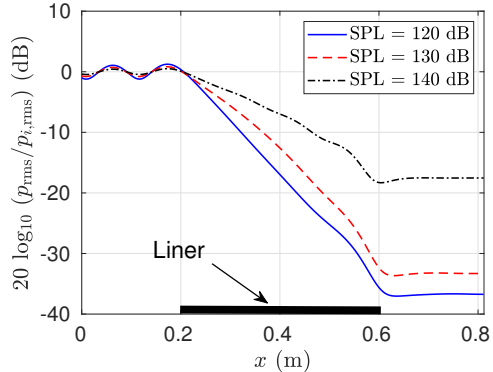


Figure 24: Variation along the wall opposite to the liner of the SPL for three incident SPL of 120, 130 and 140 dB with a harmonic excitation at  $f = 1600$  Hz.

The evolution of the SPL along the wall opposite to the liner is plotted in Fig. 24 for three incident SPL. It is seen that the SPL varies in a similar manner for the three incident SPL: it is approximately constant in the rigid sections and decreases almost linearly in the lined section. The attenuation due to the liner however depends significantly on the incident SPL: it is quite similar for incident SPL of 120 dB and 130 dB, with a value of 36 dB and 33 dB, respectively, but suffers a dramatic reduction to 18 dB for an incident SPL of 140 dB.

1  
2  
3  
4  
5  
6  
7  
8  
9  
10  
11  
12  
13  
14  
15  
16  
17  
18  
19  
20  
21  
22  
23  
24  
25  
26  
27  
28  
29  
30  
31  
32  
33  
34  
35  
36  
37  
38  
39  
40  
41  
42  
43  
44  
45  
46  
47  
48  
49  
50  
51  
52  
53  
54  
55  
56  
57  
58  
59  
60  
61  
62  
63  
64  
65

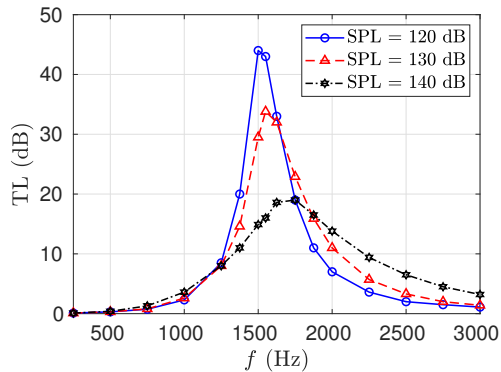


Figure 25: Transmission loss versus frequency for a harmonic excitation with incident SPL of 120, 130 and 140 dB.

600 In order to characterize the variation of the attenuation with the driving frequency, the trans-  
601 mission loss (TL) is determined from the numerical solution. The plane wave mode is the only  
602 propagating mode in the rigid sections, as the driving frequencies are below the duct cutoff fre-  
603 quency. Thus, the transmission loss can be calculated with:

$$TL = 20 \log_{10} \left( \frac{p_{i,rms}}{p_{t,rms}} \right) \quad (30)$$

604 where  $p_{t,rms}$  is the rms value of the transmitted wave amplitude in the exit section. As an anechoic  
605 termination is considered,  $p_{t,rms}$  is simply calculated from the acoustic pressure at a point sufficiently  
606 far from the liner. The transmission loss is shown for three incident SPL in Fig. 25. It is seen that  
607 increasing the incident SPL tends to widen the TL peak and reduce its amplitude. The TL peak is  
608 observed near the resonant frequency of the liner and is shifted towards higher frequencies with the  
609 increase of the incident SPL. Note that the TL peak is not at the resonant frequency of the liner  
610 because the optimal impedance at grazing incidence and for a liner of finite length is not equal to  
611 that at normal incidence.

### 612 5.2.2. Influence of the impedance spatial variation

613 An additional study is performed to investigate more precisely the influence of the impedance  
614 modeling on the prediction of sound propagation and attenuation in a lined duct under high level  
615 of excitation. To do so, three models of the liner are considered: first, the reference model with a  
616 spatially-varying nonlinear impedance model that accounts for the variation of  $v_{rms}$  along the liner,  
617 i.e.  $Z_{NL}[\omega, v_{rms}(x)]$ , second, a uniform impedance model using the nonlinear impedance model but  
618 for a constant and representative value of  $v_{rms}$  and third, the linear impedance model. Simulations

are performed for an incident SPL of 130 dB.

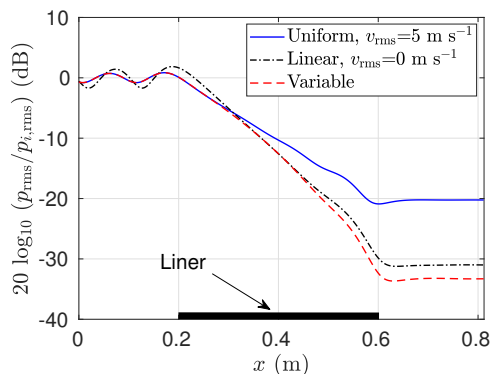


Figure 26: Variation along the wall opposite to the liner of the SPL for an incident SPL of 130 dB with a harmonic excitation at  $f = 1600$  Hz: spatially variable admittance (red dashed line), linear admittance (black dashed-dotted line) and spatially uniform admittance with  $v_{\text{rms}} = 5 \text{ m s}^{-1}$  (blue solid line)

The SPL variation along the wall opposite to the liner is depicted in Fig. 26 for a frequency of 1600 Hz and for the three liner models. Note that as the rms velocity in the perforations is about  $5 \text{ m s}^{-1}$  at the beginning in the liner for this frequency and for the incident SPL of 130 dB using the nonlinear impedance model (see Fig. 22), this value was chosen to determine the impedance in the uniform case. It is seen that the SPL prediction is significantly different for the three liner models. In particular, the SPL for a uniform impedance with  $v_{\text{rms}} = 5 \text{ m s}^{-1}$  is superimposed with that for a spatially-varying impedance for  $x < 0.3 \text{ m}$  but is then substantially smaller. The results for the linear model differ from those with the nonlinear model but a better estimation is obtained in the exit section than with the uniform case for this particular frequency and incident SPL.

Fig. 27 shows the transmission loss as a function of the frequency for the three liner models. The effect of the SPL on the transmission loss, shown in Fig. 25 discussed in Sec 5.2.1, is here observed by comparing the TL between the linear and nonlinear impedance model: the TL peak is wider and shifted towards high frequencies and its amplitude is reduced for the nonlinear impedance model compared to the linear one. In addition, the TL determined for the spatially-varying impedance model and for the uniform impedance model dramatically differs; assuming a uniform impedance leads to an under-prediction of the TL peak amplitude and an over-prediction of the peak width and of the frequency at the peak.

Two conclusions can be drawn from this example. First, neglecting nonlinear effects on the response of a perforated plate can lead to a dramatic error on the prediction of the liner attenuation.

1  
2  
3  
4  
5  
6  
7  
8  
9  
10  
11  
12  
13  
14  
15  
16  
17  
18  
19  
20  
21  
22  
23  
24  
25  
26  
27  
28  
29  
30  
31  
32  
33  
34  
35  
36  
37  
38  
39  
40  
41  
42  
43  
44  
45  
46  
47  
48  
49  
50  
51  
52  
53  
54  
55  
56  
57  
58  
59  
60  
61  
62  
63  
64  
65

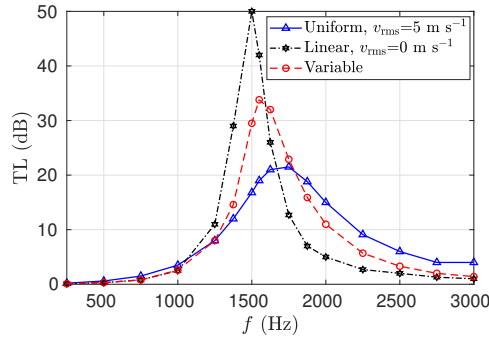


Figure 27: Comparison of the transmission loss for an incident SPL of 130 dB between three cases: spatially variable admittance (red), linear admittance (black) and spatially uniform admittance with  $v_{\text{rms}} = 5 \text{ m s}^{-1}$  (blue)

639 Second, the spatial variations of the parameter governing the nonlinear effect on the liner impedance  
 640 (here  $v_{\text{rms}}$ ) should be taken into account for an accurate modeling of the liner acoustic properties  
 641 and that assuming a constant value for the impedance at high SPL might be a rough approximation.

642 *5.3. Broadband excitation*

643 Finally, the case of an incident broadband signal is considered for different incident SPL.

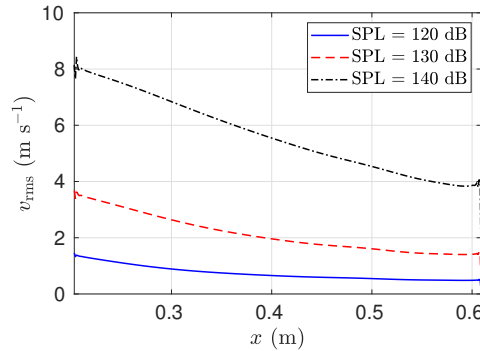


Figure 28: Variation along the liner of the rms velocity for three incident SPL of 120, 130 and 140 dB with a broadband excitation.

644 The rms amplitude of the velocity in the perforations is plotted along the liner in Fig. 28.  
 645 Compared to the harmonic excitation at  $f = 1600 \text{ Hz}$  for the same incident SPL in Fig. 22,  $v_{\text{rms}}$   
 646 is in the same order of magnitude and similarly reduces along the liner. However, it decreases at a  
 647 lower rate and its value at the beginning of the liner is **smaller**. For this given liner length,  $v_{\text{rms}}$  for  
 648 the broadband excitation is thus smaller than that for the harmonic excitation in the first part of

the lined section and larger in the second part.

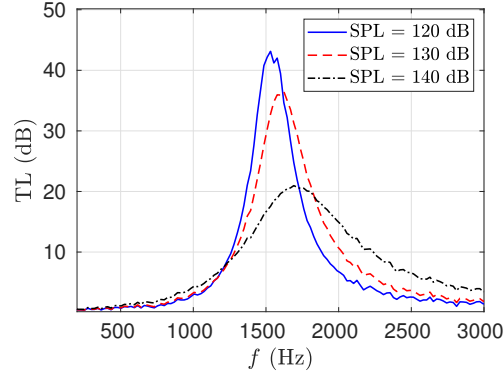


Figure 29: Transmission loss versus frequency for a broadband excitation with incident SPL of 120, 130 and 140 dB.

Fig. 29 shows the transmission loss in the case of the broadband signal. It is determined with:

$$TL = 10 \log_{10} \left( \frac{S_{ii}}{S_{tt}} \right) \quad (31)$$

where  $S_{ii}$  and  $S_{tt}$  are the power spectral densities of the incident and transmitted pressure signal, respectively. The evolution of the TL for the broadband excitation is similar to that observed for the harmonic excitation in Fig. 25. Actually, the TL for PP#1 and for the three incident SPL are, remarkably, almost identical for both types of excitation: thus, the width and amplitude of the TL peak is similar and it is observed near the same frequencies. While this should be the case in the linear regime, it is seen that, for this particular liner, the liner attenuation does not depend significantly on the type of excitation. Some differences in the TL can however be noticed. For example, the TL at  $f = 1600$  Hz for an incident SPL of 130 dB is equal to 32 dB for a harmonic excitation but to 36 dB for the broadband excitation. In addition, the maximum of TL is observed near a frequency of 1600 Hz for the broadband excitation but near 1550 Hz for a harmonic excitation.

A thorough analysis of the difference in the acoustic propagation along a lined duct depending on the type of excitation remains to be done and can be the subject of future research.

## 6. Conclusion

Time-domain admittance boundary conditions in the nonlinear regime were investigated to model the acoustic behavior of liners under a high excitation level. A particular focus was brought

1  
2  
3  
4 667 on perforated plate liners. The nonlinear model of Laly *et al.* [12] was employed for that. It  
5  
6 668 accounts for the variation of the surface admittance with the frequency and the rms velocity in the  
7  
8 669 perforation.

9  
10 670 Two extensions of the TDABC proposed by Troian *et al.* [24] in the linear regime were con-  
11  
12 671 sidered. They are both based on a multipole model, so that the TDABC can be evaluated by  
13  
14 672 integrating ODEs. The variation of the surface admittance with the rms velocity is dealt with  
15  
16 673 by interpolation from a set of reference values. They however differ on the interpolation process.  
17  
18 674 The first nonlinear TDABC, referred to as the IA method and proposed by Shur *et al.* [26], is  
19  
20 675 based on the direct interpolation of the admittance. The IA method thus requires to determine  
21  
22 676 a multipole approximation of the surface admittance model for each reference value; the number  
23  
24 677 of poles of the corresponding nonlinear multipole model is therefore considerably larger than the  
25  
26 678 linear counterpart. In the second nonlinear TDABC, called the IAP method, interpolation of the  
27  
28 679 multipole function coefficients is preferred. This allows for a large reduction in the number of poles  
29  
30 680 compared to the IA method.

31 681 The two methods were implemented in a finite-difference time-domain solver of the linearized  
32  
33 682 Euler equations. Numerical experiments and comparisons with measurements on an impedance  
34  
35 683 tube configuration were performed for validation and evaluation purposes. Three PP liners were  
36  
37 684 considered for a harmonic and a broadband excitation. It was shown that the IA and IAP methods  
38  
39 685 allow both for an accurate and efficient representation of the surface admittance in the nonlinear  
40  
41 686 regime. Depending on the situation, one of the two methods is preferable. When considering  
42  
43 687 analytical models for which the admittance varies smoothly with the frequency, a multipole func-  
44  
45 688 tion with only two poles is sufficient to accurately represent the admittance. Since the IAP has  
46  
47 689 the smallest computational cost (because of the smallest number of poles), it may be preferred  
48  
49 690 over the IA method in this case. When considering experimental admittance data, the multipole  
50  
51 691 representation may require a significantly larger (5 to 8) number of poles in order to achieve ac-  
52  
53 692 ceptable accuracy. With such number of poles, the IAP approach may well become inaccurate  
54  
55 693 because of the high sensitivity of the multipole function to the location of the poles and may lead  
56  
57 694 to non-physical results, such a negative resistance over a given frequency band. Furthermore, the  
58  
59 695 admittance approximation with a decent accuracy may require using different number of poles  
60  
61 696 for different reference values of  $v_{\text{rms}}$ ; this is not possible with the current formulation of the IAP  
62  
63 697 method. For such cases, the IA method may be superior.

64  
65 698 Finally, the proposed TDABC was applied to sound propagation along a 2D lined duct under

1  
2  
3  
4 699 high level of excitation. It was exemplified that the spatial variations of the surface impedance are  
5  
6 700 significant near the resonant frequency of the liner and has to be taken into account for an accurate  
7  
8 701 prediction of liner attenuation at high SPL.

9  
10 702 There are several ways to pursue this study. The simulations have been restricted to a medium  
11  
12 703 at rest. Future work will consider the effect of a mean flow. Besides, along impedance tube  
13  
14 704 measurements, it will be interesting to have a detailed acoustic database on a duct lined with a PP  
15  
16 705 absorber for benchmarking. In addition, the concept of optimal impedance has been developed for  
17  
18 706 a lined duct with a uniform impedance. **It should be extended** to the case of a spatially-varying  
19  
20 707 impedance to be applicable to perforated liners at high level of excitation. Finally, a methodology  
21  
22 708 to account for extended-reacting liners in time-domain simulations has been recently proposed in  
23  
24 709 Alomar *et al.* [42]. In particular, perforated liners with a back cavity were considered by modelling  
25  
26 710 the perforated plate by an impedance jump. Following the nonlinear TDABC investigated in this  
27  
28 711 paper, it would be also possible to extend this methodology for perforated liners in the nonlinear  
29  
30 712 regime.

## 31 **Appendix A. Coefficients of the nonlinear TDABC**

32  
33  
34 714 This appendix provides the coefficients of the nonlinear TDABC for the PP#1 absorber with  
35  
36 715 two cavity depths 10 and 30 mm. The Laly model for this liner is approximated by a single pair  
37  
38 716 of complex conjugate poles  $\lambda_1$  and  $\lambda_2 = \lambda_1^*$ , with  $A_2 = A_1^*$  over the range of velocities in the  
39  
40 717 perforations considered in this paper.

41  
42 718 For the interpolation of the admittance (IA) method, the poles and the coefficients of the  
43  
44 719 multipole model (see Eq. (13)) are given for the different reference values of the rms velocity in the  
45  
46 720 perforations in Tab. A.4.

46 721 For the interpolation of the admittance parameters (IAP) method, the poles and the coefficients  
47  
48 722 (see Eq. (22)) are approximated by a rational function with quadratic polynomials, that can be  
49  
50 723 written as follows:

$$51 \quad X(v_{\text{rms}}) = \frac{a + b v_{\text{rms}} + c v_{\text{rms}}^2}{1 + d v_{\text{rms}} + e v_{\text{rms}}^2}. \quad (\text{A.1})$$

52  
53  
54 724 The constants  $a$ ,  $b$ ,  $c$ ,  $d$  and  $e$  are given for each coefficient of the multipole model in Tab. A.5.

## 57 **Appendix B. Additional comparisons with impedance tube experiments for broad-** 58 59 **band excitation**

1  
2  
3  
4  
5  
6  
7  
8  
9  
10  
11  
12  
13  
14  
15  
16  
17  
18  
19  
20  
21  
22  
23  
24  
25  
26  
27  
28  
29  
30  
31  
32  
33  
34  
35  
36  
37  
38  
39  
40  
41  
42  
43  
44  
45  
46  
47  
48  
49  
50  
51  
52  
53  
54  
55  
56  
57  
58  
59  
60  
61  
62  
63  
64  
65

<b>PP#1, Cavity depth of 10 mm</b>						
Reference rms velocity (m s <sup>-1</sup> )	2	4	6	8	10	12
Re[A <sub>1</sub> ]	1.680e+03	1.840e+03	1.962e+03	2.035e+03	2.085e+03	2.129e+03
Im[A <sub>1</sub> ]	2.827e+02	4.331e+02	6.624e+02	9.044e+02	1.162e+03	1.532e+03
Re[λ <sub>1</sub> ] (s <sup>-1</sup> )	1.609e+03	2.504e+03	3.675e+03	4.770e+03	5.795e+03	7.029e+03
Im[λ <sub>1</sub> ] (s <sup>-1</sup> )	-1.054e+04	-1.091e+04	-1.096e+04	-1.076e+04	-1.041e+04	-9.776e+03
Y <sub>∞</sub>	4.0492e-03	1.7636e-03	7.288e-04	3.7514e-04	2.231e-04	1.315e-04

<b>PP#1, Cavity depth of 30 mm</b>						
Reference rms velocity (m s <sup>-1</sup> )	2	4	6	8	10	12
Re[A <sub>1</sub> ]	1.552e+03	1.700e+03	1.803e+03	1.861e+03	1.900e+03	1.933e+03
Im[A <sub>1</sub> ]	3.983e+02	6.782e+02	1.115e+03	1.675e+03	2.547e+03	6.661e+03
Re[λ <sub>1</sub> ] (s <sup>-1</sup> )	1.418e+03	2.290e+03	3.369e+03	4.359e+03	5.280e+03	6.382e+03
Im[λ <sub>1</sub> ] (s <sup>-1</sup> )	-5.771e+03	-5.792e+03	-5.460e+03	-4.849e+03	-3.940e+03	-1.852e+03
Y <sub>∞</sub>	4.949e-03	1.723e-03	6.431e-04	3.223e-04	1.921e-04	1.154e-04

Table A.4: Poles and coefficients of the multipole model for the interpolation of the admittance (IA) method.

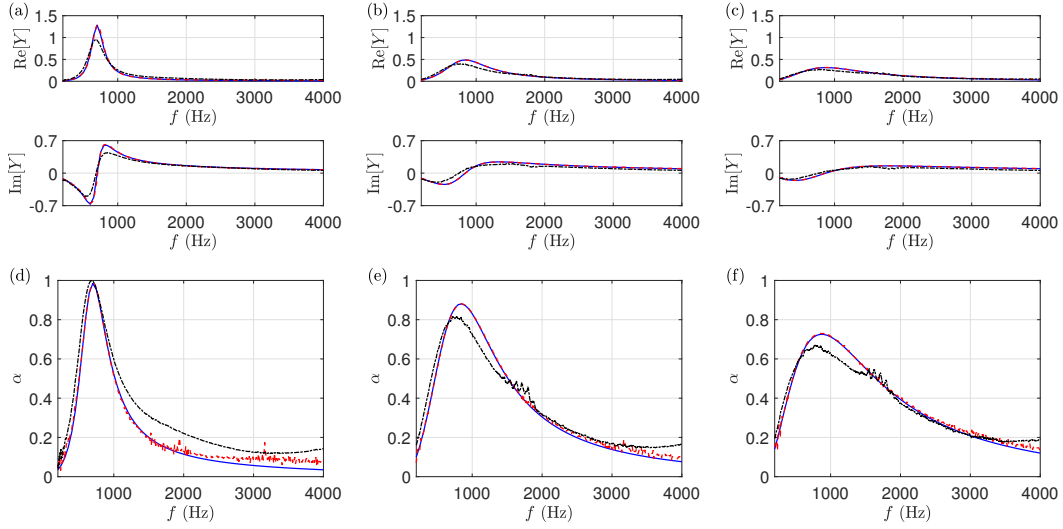
<b>PP#1, Cavity depth of 10 mm</b>					
X	Re[A <sub>1</sub> ]	Im[A <sub>1</sub> ]	Re[λ <sub>1</sub> ] (s <sup>-1</sup> )	Im[λ <sub>1</sub> ] (s <sup>-1</sup> )	Y <sub>∞</sub>
a	1.430e+03	1.965e+02	9.911e+02	-9.678e+03	2.379e-04
b	5.176e+02	3.294e+01	3.717e+02	-1.054e+03	-5.229e-03
c	1.033e+02	9.665e+00	1.853e+02	4.519e+01	4.199e-02
d	2.746e-01	2.404e-02	2.785e-01	5.174e-02	5.924e-01
e	4.354e-02	9.060e-08	1.431e-03	3.785e-08	3.499e+00

<b>PP#1, Cavity depth of 30 mm</b>					
X	Re[A <sub>1</sub> ]	Im[A <sub>1</sub> ]	Re[λ <sub>1</sub> ] (s <sup>-1</sup> )	Im[λ <sub>1</sub> ] (s <sup>-1</sup> )	Y <sub>∞</sub>
a	1.308e+03	1.738e+02	7.187e+02	-5.398e+03	1.310e-02
b	8.897e+02	8.252e+01	4.897e+02	1.402e+01	-1.615e-03
c	3.224e+02	-6.832e+00	2.652e+02	2.951e+01	7.271e-05
d	6.127e-01	-1.235e-01	4.883e-01	-3.844e-02	5.355e-02
e	1.517e-01	3.524e-03	8.734e-04	3.995e-09	2.183e-01

Table A.5: Constants of the rational functions used for the coefficients of the multipole model with the interpolation of the admittance parameters (IAP) method.

1  
2  
3  
4 727 In this appendix, additional comparisons between the impedance tube measurements for a  
5  
6 728 broadband excitation and corresponding numerical results are presented. The experimental set-up  
7  
8 729 is described in Sec. 4.3 and the procedure used for the numerical simulations is detailed in Sec. 4.3.2.  
9



10  
11  
12  
13  
14  
15  
16  
17  
18  
19  
20  
21  
22  
23  
24  
25  
26  
27  
28  
29  
30  
31 Figure B.30: (top) Surface admittance and (bottom) absorption coefficient of PP#2 absorber with a cavity depth of  
32  
33 30 mm for a broadband excitation and for three incident SPL (a)-(d) 76.8 dB, (b)-(e) 126.5 dB and (c)-(f) 133.4 dB:  
34 measured (black dash-dotted) and determined from the analytical model in Eq. (3) (blue solid) and from the numerical  
35 solution (red dashed).  
36  
37

38  
39 730 Fig. B.30 shows the surface admittance and the absorption coefficient for PP#2 with a cavity  
40  
41 731 depth of 30 mm and for three incident sound pressure levels. The experimental results are quali-  
42  
43 732 tatively similar to those obtained for PP#1 in Figs. 18 and 19. The increase of the incident sound  
44  
45 733 pressure level leads to a flattening of the admittance curves and a reduction and a broadening of  
46  
47 734 the absorption peak. The results obtained with the numerical simulations do not match exactly  
48  
49 735 the experimental curves, but the evolution of the admittance and the absorption coefficient with  
50  
51 736 the incident SPL is correctly reproduced. Note also that the numerical results provide a close  
52  
53 737 agreement with the analytical model.  
54

55 738 Corresponding results for PP#3 with a cavity depth of 30 mm are plotted in Fig. B.31. In this  
56  
57 739 case also, the experimental admittance curves tends to flatten with the increase of the incident SPL.  
58  
59 740 Nevertheless, the absorption coefficient behaves differently. The absorption coefficient significantly  
60  
61 741 rises with the increase of the incident SPL from 76.6 dB to 125.3 dB. Then, the peak value decreases  
62  
63 742 and the absorption peak broadens with a further increase of the incident SPL up to 133.5 dB. The  
64  
65

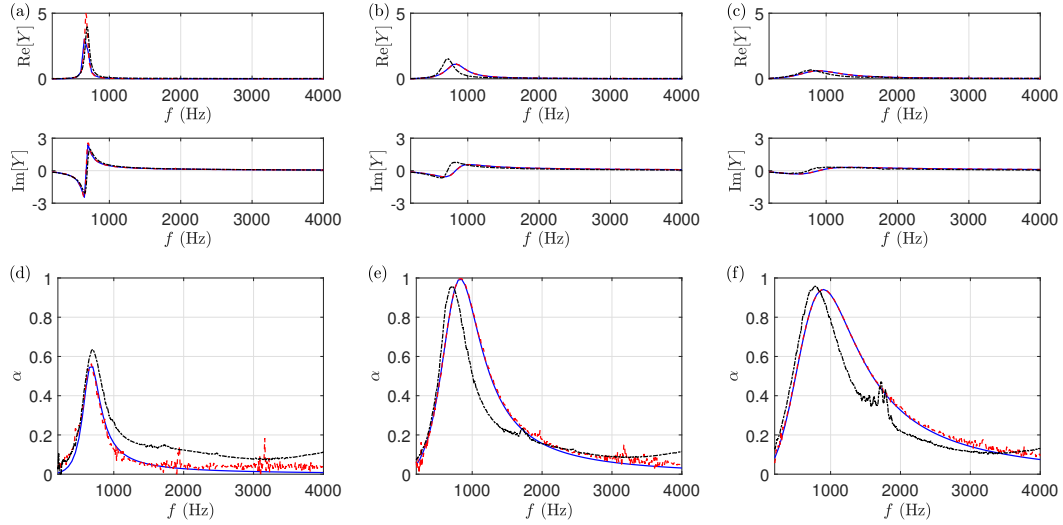


Figure B.31: (top) Surface admittance and (bottom) absorption coefficient of PP#3 absorber with a cavity depth of 30 mm for a broadband excitation and for three incident SPL (a)-(d) 76.6 dB, (b)-(e) 125.3 dB and (c)-(f) 133.5 dB: measured (black dash-dotted) and determined from the analytical model in Eq. (3) (blue solid) and from the numerical solution (red dashed).

numerical simulations predict the overall evolution of the admittance and the absorption coefficient with the increase of the incident SPL. Discrepancies are however noticeable for this PP absorber. For the incident SPL of 125.3 dB, the peak in  $\text{Re}[Y]$  is thus predicted at a higher frequency. The absorption peak is also shifted towards high frequencies with the increase of the SPL, while it is centered around a frequency independent of the incident SPL in the experiments. In addition, the results from the analytical model and from the numerical simulations show a close agreement.

Finally, Tab. B.6 indicates the rms amplitude of the velocity in the perforations for PP#2 and PP#3 with a cavity depth of 30 mm determined from the measurements and from the numerical simulations. While a decent prediction is noticed, the value of  $v_{\text{rms}}$  tends to be overestimated in the numerical simulations, in particular in the linear regime. In the nonlinear regime, the differences between the values determined from the experiments and the numerical simulations reduce. Thus,  $v_{\text{rms}}$  is accurately predicted with an error smaller than 5% for the largest incident SPL.

## Acknowledgments

This work was performed within the framework of the Labex CeLyA of the University of Lyon, within the program “Investissements d’Avenir” (ANR-10-LABX-0060/ANR-16-IDEX-0005) oper-

1  
2  
3  
4  
5  
6  
7  
8  
9  
10  
11  
12  
13  
14  
15  
16  
17  
18  
19  
20  
21  
22  
23  
24  
25  
26  
27  
28  
29  
30  
31  
32  
33  
34  
35  
36  
37  
38  
39  
40  
41  
42  
43  
44  
45  
46  
47  
48  
49  
50  
51  
52  
53  
54  
55  
56  
57  
58  
59  
60  
61  
62  
63  
64  
65

**PP#2, Cavity depth of 30 mm**

Incident SPL (dB)		76.8	86.5	97.2	106.7	116.5	126.5	133.4
$v_{\text{rms}}$ (m s <sup>-1</sup> )	exp.	$1.59 \times 10^{-2}$	$4.59 \times 10^{-2}$	$1.56 \times 10^{-1}$	$4.58 \times 10^{-1}$	1.35	3.78	7.13
	num.	$1.93 \times 10^{-2}$	$6.17 \times 10^{-2}$	$2.16 \times 10^{-1}$	$6.02 \times 10^{-1}$	1.60	4.03	7.16

**PP#3, Cavity depth of 30 mm**

Incident SPL (dB)		76.6	86.6	96.4	106.2	116.1	125.3	133.5
$v_{\text{rms}}$ (m s <sup>-1</sup> )	exp.	$1.24 \times 10^{-2}$	$3.73 \times 10^{-2}$	$1.15 \times 10^{-1}$	$3.55 \times 10^{-1}$	1.07	2.84	6.43
	num.	$2.23 \times 10^{-2}$	$7.34 \times 10^{-2}$	$2.17 \times 10^{-1}$	$6.19 \times 10^{-1}$	1.70	3.52	6.61

Table B.6: Rms amplitude of the velocity in the perforations for PP#2 and PP#3 absorbers with a cavity depth of 30 mm for a broadband excitation: values deduced from the experiments and from the numerical simulations.

ated by the French National Research Agency. This project has received funding from the Clean Sky  
2 Joint Undertaking under the European Union’s Horizon 2020 research and innovation programme  
under grant agreement N°821093 (SALUTE).

**References**

[1] L. Sivian, Acoustic impedance of small orifices, Journal of the Acoustical Society of America 7 (1935) 94–101.

[2] C. K. W. Tam, H. Ju, M. G. Jones, W. R. Watson, T. L. Parrott, A computational and experimental study of resonators in three dimensions, Journal of Sound and Vibration 329 (2010) 5164–5193.

[3] Q. Zhang, D. J. Bodony, Numerical investigation and modelling of acoustically excited flow through a circular orifice backed by a hexagonal cavity, Journal of Fluid Mechanics 693 (2012) 367–401.

[4] A. W. Guess, Calculation of perforated plate liner parameters from specified acoustic resistance and reactance, Journal of Sound and Vibration 40 (1975) 119–137.

[5] D.-Y. Maa, Potential of microperforated panel absorber, Journal of the Acoustical Society of America 104 (1998) 2861–2866.

1  
2  
3  
4  
5  
6  
7  
8  
9  
10  
11  
12  
13  
14  
15  
16  
17  
18  
19  
20  
21  
22  
23  
24  
25  
26  
27  
28  
29  
30  
31  
32  
33  
34  
35  
36  
37  
38  
39  
40  
41  
42  
43  
44  
45  
46  
47  
48  
49  
50  
51  
52  
53  
54  
55  
56  
57  
58  
59  
60  
61  
62  
63  
64  
65

774 [6] A. Hersh, B. Walker, J. Celano, Helmholtz resonator impedance model, part 1: nonlinear  
775 behavior, *AIAA Journal* 41 (2003) 795–808.

776 [7] H. Bodén, Y. Guo, H. B. Töziün, Experimental investigation of nonlinear acoustic proper-  
777 ties for perforates, 12th AIAA/CEAS Aeroacoustics Conference (27th AIAA Aeroacoustics  
778 Conference), Cambridge, MA, USA, 8-10 May, 2006, AIAA Paper 2006-2404, p. 1–8.

779 [8] R. Tayong, T. Dupont, P. Leclaire, On the variations of acoustic absorption peak with particle  
780 velocity in micro-perforated panels at high level of excitation, *Journal of the Acoustical Society of  
781 America* 127 (2010) 2875–2882.

782 [9] S.-H. Park, A design method of micro-perforated panel absorber at high sound pressure envi-  
783 ronment in launcher fairings, *Journal of Sound and Vibration* 332 (2013) 521–535.

784 [10] U. Ingard, H. Ising, Acoustic nonlinearity of an orifice, *Journal of the Acoustical Society of  
785 America* 42 (1967) 6–17.

786 [11] T. H. Melling, The acoustic impedance of perforates at medium and high sound pressure  
787 levels, *Journal of Sound and Vibration* 29 (1973) 1–65.

788 [12] Z. Laly, N. Atalla, S.-A. Meslioui, Acoustical modeling of micro-perforated panel at high  
789 sound pressure levels using equivalent fluid approach, *Journal of Sound and Vibration* 427  
790 (2018) 134–158.

791 [13] N. Atalla, F. Sgard, Modeling of perforated plates and screens using rigid frame porous models,  
792 *Journal of Sound and Vibration* 303 (2007) 195–208.

793 [14] A. Cummings, Transient and multiple frequency sound transmission through perforated plates  
794 at high amplitude, *Journal of the Acoustical Society of America* 74 (1986) 942–951.

795 [15] W. Eversman, Effect of local impedance variation and non-linearity on multiple tone attenu-  
796 ation, *International Journal of Aeroacoustics* 14 (2015) 281–303.

797 [16] R. Roncen, F. Méry, E. Piot, P. Klotz, Spatially-varying impedance model for locally reacting  
798 acoustic liners at a high sound intensity, *Journal of Sound and Vibration* 524, 116741 (2022)  
799 1–19.

800 [17] Y. Özyörük, L. Long, A time-domain implementation of surface acoustic impedance condition  
801 with and without flow, *Journal of Computational Acoustics* 5 (1997) 277–296.

1  
2  
3  
4  
5  
6  
7  
8  
9  
10  
11  
12  
13  
14  
15  
16  
17  
18  
19  
20  
21  
22  
23  
24  
25  
26  
27  
28  
29  
30  
31  
32  
33  
34  
35  
36  
37  
38  
39  
40  
41  
42  
43  
44  
45  
46  
47  
48  
49  
50  
51  
52  
53  
54  
55  
56  
57  
58  
59  
60  
61  
62  
63  
64  
65

[18] C. K. W. Tam, L. Auriault, Time-domain impedance boundary conditions for computational  
aeroacoustics, *AIAA Journal* 34 (1996) 917–923.

[19] K. Y. Fung, H. Ju, Broadband time-domain impedance models, *AIAA Journal* 39 (2001)  
1449–1454.

[20] C. Richter, F. H. Thiele, X. D. Li, M. Zhuang, Comparison of time-domain impedance bound-  
ary conditions for lined duct flows, *AIAA Journal* 45 (2007) 1933–1945.

[21] F. Monteghetti, D. Matignon, E. Piot, L. Pascal, Design of broadband time-domain impedance  
boundary conditions using the oscillatory-diffusive representation of acoustical models, *Journal  
of the Acoustical Society of America* 140 (2016) 1663–1674.

[22] Y. Reymen, M. Baelmans, W. Desmet, Efficient implementation of Tam and Auriault’s time-  
domain impedance boundary condition, *AIAA Journal* 46 (2008) 2368–2376.

[23] X. Y. Li, X. D. Li, C. K. W. Tam, Improved multipole broadband time-domain impedance  
boundary condition, *AIAA Journal* 50 (2012) 980–984.

[24] R. Troian, D. Dragna, C. Bailly, M.-A. Galland, Broadband liner impedance eduction for mul-  
timodal acoustic propagation in the presence of a mean flow, *Journal of Sound and Vibration*  
392 (2017) 200–216.

[25] D. Dragna, P. Pineau, P. Blanc-Benon, A generalized recursive convolution method for time-  
domain propagation in porous media, *Journal of the Acoustical Society of America* 138 (2015)  
1030–1042.

[26] M. Shur, M. Strelets, A. Travin, T. Suzuki, P. Spalart, Unsteady simulations of sound propa-  
gation in turbulent flow inside a lined duct, *AIAA Journal* 59 (2021) 3054–3070.

[27] J. Allard, N. Atalla, *Propagation of sound in porous media: modelling sound absorbing mate-  
rials*, Second edition, John Wiley & Sons, 2009.

[28] Z. Laly, N. Atalla, S.-A. Meslioui, K. El Bikri, Sensitivity analysis of micro-perforated panel  
absorber models at high sound pressure levels, *Applied Acoustics* 156 (2019) 7–20.

[29] C. Bogey, C. Bailly, A family of low dispersive and low dissipative explicit schemes for flow  
and noise computations, *Journal of Computational Physics* 194 (2004) 194–214.

1  
2  
3  
4  
5  
6  
7  
8  
9  
10  
11  
12  
13  
14  
15  
16  
17  
18  
19  
20  
21  
22  
23  
24  
25  
26  
27  
28  
29  
30  
31  
32  
33  
34  
35  
36  
37  
38  
39  
40  
41  
42  
43  
44  
45  
46  
47  
48  
49  
50  
51  
52  
53  
54  
55  
56  
57  
58  
59  
60  
61  
62  
63  
64  
65

829 [30] J. Berland, C. Bogey, O. Marsden, C. Bailly, High-order, low dispersive and low dissipative  
830 explicit schemes for multiple-scale and boundary problems, *Journal of Computational Physics*  
831 224 (2007) 637 – 662.

832 [31] J. Berland, C. Bogey, C. Bailly, Low-dissipation and low-dispersion fourth-order Runge–Kutta  
833 algorithm, *Computers & Fluids* 35 (2006) 1459–1463.

834 [32] C. Bogey, N. De Cacqueray, C. Bailly, A shock-capturing methodology based on adaptative  
835 spatial filtering for high-order non-linear computations, *Journal of Computational Physics* 228  
836 (2009) 1447–1465.

837 [33] F. Monteghetti, D. Matignon, E. Piot, Energy analysis and discretization of nonlinear  
838 impedance boundary conditions for the time-domain linearized Euler equations, *Journal of*  
839 *Computational Physics* 375 (2018) 393–426.

840 [34] B. Gustavsen, A. Semlyen, Rational approximation of frequency domain responses by vector  
841 fitting, *IEEE Transactions on Power Delivery* 14 (1999) 1052–1061.

842 [35] R. Billard, Study of perforated liners for aeronautics, Ph.D. thesis, Le Mans Université, 2021.

843 [36] K. U. Ingard, *Theoretical acoustics*, McGraw Hill, 1968.

844 [37] J. Chung, D. Blaser, Transfer function method of measuring in-duct acoustic properties. i.  
845 theory, *Journal of the Acoustical Society of America* 68 (1980) 907–913.

846 [38] B. S. Beck, N. H. Schiller, M. G. Jones, Impedance assessment of a dual-resonance acoustic  
847 liner, *Applied Acoustics* 93 (2015) 15–22.

848 [39] M. G. Jones, W. R. Watson, T. L. Parrott, Benchmark data for evaluation of aeroacoustic  
849 propagation codes with grazing flow, 11th AIAA/CEAS Aeroacoustics Conference, Monterey,  
850 CA, USA, 23-25 May, 2005, AIAA Paper 2005-2853, p. 1–18.

851 [40] V. Lafont, F. Méry, R. Roncen, F. Simon, E. Piot, Liner impedance eduction under shear  
852 grazing flow at a high sound pressure level, *AIAA Journal* 58 (2020) 1107–1117.

853 [41] C. Chen, X. Li, F. Hu, On spatially varying acoustic impedance due to high sound intensity  
854 decay in a lined duct, *Journal of Sound and Vibration* 483, 115430 (2020) 1–28.

1  
2  
3  
4  
5  
6  
7  
8  
9  
10  
11  
12  
13  
14  
15  
16  
17  
18  
19  
20  
21  
22  
23  
24  
25  
26  
27  
28  
29  
30  
31  
32  
33  
34  
35  
36  
37  
38  
39  
40  
41  
42  
43  
44  
45  
46  
47  
48  
49  
50  
51  
52  
53  
54  
55  
56  
57  
58  
59  
60  
61  
62  
63  
64  
65

855 [42] A. Alomar, D. Dragna, M.-A. Galland, Time-domain simulations of sound propagation in a  
856 flow duct with extended-reacting liners, *Journal of Sound and Vibration* 507, 116137 (2021)  
857 1–24.

**Daher Diab:** Conceptualization, Methodology, Validation, Experiments, Investigation, Writing – original draft, Writing – review & editing.

**Didier Dragna:** Conceptualization, Methodology, Writing – original draft, Formal analysis.

**Edouard Salze:** Conceptualization, Methodology, Validation, Experiments, Investigation. Marie-

**Annick Galland:** Conceptualization, Methodology, Writing – review & editing, Supervision, Funding acquisition.

**Declaration of interests**

The authors declare that they have no known competing financial interests or personal relationships that could have appeared to influence the work reported in this paper.

The authors declare the following financial interests/personal relationships which may be considered as potential competing interests: